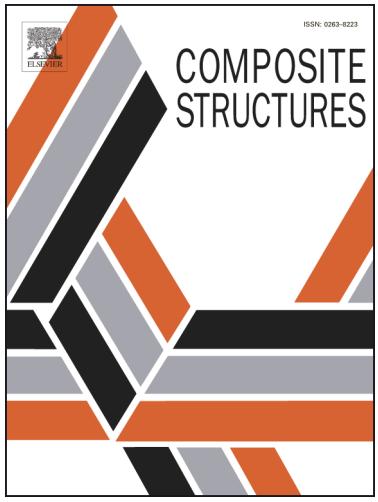

Isogeometric analysis for size-dependent nonlinear thermal stability of porous FG microplates

Cuong-Le Thanh, Loc V. Tran, Tinh Quoc Bui, Hoang X. Nguyen, M. Abdel-Wahab

PII: S0263-8223(19)30292-2
DOI: https://doi.org/10.1016/j.compstruct.2019.04.010
Reference: COST 10838

To appear in: *Composite Structures*

Received Date: 24 January 2019
Revised Date: 11 March 2019
Accepted Date: 3 April 2019

Please cite this article as: Thanh, C-L., Tran, L.V., Quoc Bui, T., Nguyen, H.X., Abdel-Wahab, M., Isogeometric analysis for size-dependent nonlinear thermal stability of porous FG microplates, *Composite Structures* (2019), doi: https://doi.org/10.1016/j.compstruct.2019.04.010

Isogeometric analysis for size-dependent nonlinear thermal stability of porous FG microplates

Cuong-Le Thanh[a,b], Loc V. Tran [f], Tinh Quoc Bui[g], Hoang X. Nguyen[h], M. Abdel-Wahab[c,d]*

[a]Department of Electrical energy, metals, mechanical constructions and systems, Soete Laboratory, Faculty of Engineering and Architecture, Ghent University, Belgium
[b]Faculty of Civil Engineering and Electricity, Open University, Ho Chi Minh City, Vietnam
[c]Division of Computational Mechanics, Ton Duc Thang University, Ho Chi Minh City, Vietnam
[d]Faculty of Civil Engineering, Ton Duc Thang University, Ho Chi Minh City, Vietnam
[f]Department of Civil Engineering, School of Engineering, Aalto University, Finland
[g] Department of Civil and Environmental Engineering, Tokyo Institute of Technology 2-12-1-W8-22, Ookayama, Meguro-ku, Tokyo, 152-8552, Japan
[h]Department of Mechanical and Construction Engineering, Northumbria University, Newcastle upon Tyne NE1 8ST, United Kingdom

* Corresponding author: magd.abdelwahab@tdt.edu.vn

A B S T R A C T

In this article, we present for the first time a research analysis for the size-dependent effects on thermal buckling and post-buckling behaviors of functionally graded material micro-plates with porosities (imperfect FGM) using isogeometric analysis. A seventh-order shear deformation plate theory associated with the modified couple stress theory (MCST) is particularly imposed to capture the size-dependent phenomenon within imperfect FGM micro-plates. The material properties of imperfect FGM micro-plates with three different distributions of porosities including even, uneven and logarithmic-uneven varying across the plate thickness are derived from the modified rule-of-mixture assumption. The nonlinear governing equation for size-dependent imperfect FGM micro-plate under uniform, linear and nonlinear temperature rise is derived using the Von-Kármán assumption and Hamilton's principle. Through numerical example, the effect of temperature rise, boundary conditions, power index, porosity volume fraction, porosity distribution pattern and material length scale parameter on thermal buckling and post-buckling behaviors of FGP micro-plates are investigated.

Keywords: Porosity; size-dependent; Functionally graded material micro-plates, Thermal buckling; Thermal post-buckling; modified couple stress theory; Imperfect.

1. Introduction

The earliest functionally graded materials (FGMs) were first developed by a group of Japanese researchers in the mid-1980s, which are composite materials with microscopically inhomogeneous property [1]. FGMs are formed by continuously varying the volume fraction of ceramic and metal through the thickness direction. The advantages of these materials are low thermal conductivity, less sensitive to crack and delamination, and ductility. The FGMs are now widely applied in a variety of engineering applications including automobile, nuclear energy, aerospace, electronics, biomaterials, solar energy and commodities [2-6]. During fabrication process of FGM, the porosities and micro-voids can take places inside the material as a result of technical problems [7, 8].

The existence of porosities may decrease the material strength and may greatly affect the mechanical properties of structures. This means that understanding the influence of the porosity on FGM structures is of great importance in design and manufacturing. Accordingly, linear and nonlinear analysis for imperfect FGM plate and beam with porosity have been attractive to researchers. Wattanasakulpong and Ungbhakorn [9] considered linear and nonlinear free vibration of FGM beams having porosities. They proposed the modified rule-of-mixture to approximate the material properties of FGM beam with porosity phases. Wattanasakulpong and Chaikittiratana [10] also employed the Chebyshev collocation method to investigate the porosity effect on natural frequencies of imperfect FGM Timoshenko beam with even and uneven porosity distribution through the thickness direction. Chen et al. [11] carried out the static bending and buckling analysis of porous FGM beam under different boundary conditions, where the porosity distribution is assumed to be graded through thickness's direction. Ebrahimi and Zia [12] employed Galerkin's method and multiple scale method to study nonlinear vibration behavior of FG beam made of porous material. Atmane et al. [13] also derived a closed form solutions for free vibration, static bending and buckling of FGM beam with porosities resting on elastic foundations. Akbaş [14] presented a finite element solution for nonlinear static analysis of porous FG beam under temperature rising, which is derived from heat transfer equation. By using hyperbolic shear deformation and Navier technique, a closed form solutions for vibration of FGM plate having porosities was also obtained by Mouaici et al. [15]. Barati and Zenkour [16] presented an analytical solution for free vibration of a porous FG piezoelectric plate in

thermal environment with different boundary conditions, in which the material properties of two pattern of porous distribution are assumed according to the modified power law model. Recently, Barati et al. [17] also developed an analytical solution based on refined four variables plate theory for free vibration analysis of FG piezoelectric plate with porosities. Shahsavari et al. [18] proposed a quasi-3D hyperbolic plate theory for free vibration analysis of FG plates on elastic foundation with even, uneven and logarithmic porosity distribution. Karami et al. [19] studied the wave propagation problem of porous FG nanoplate with in-plane magnetic field resting on Winkler Pasternak foundation. More recently, Pham et al. [20] derived a closed form expression for buckling and post buckling of simply supported porous FG plates on an elastic foundation. Nguyen et al. [21] developed a polygonal finite element method for geometrical nonlinear analysis of porous FG plates. A 3-D exact solution was obtained by Zhao et al. [22] for vibration analysis of porous FG rectangular plates with three different types of porosity distributions.

In recent years, a number of size-dependent elasticity models based on non-classical continuum theories have been developed [23-29] for capturing the small scale phenomena for linear and nonlinear analysis of micro-/nano-structures. For the sake of simplicity of size effect exploration, the modified couple stress (MCST) was first introduced by Yang et al. [26] based on the classical couple stress theory that proposed by Mindlin [24], Toupin [27] and Koiter [28]. In this theory, the number of material length scale parameter is reduced to one instead of two. Due to this advantage, many researchers have focused on studying the size-dependent effects on static and dynamic behaviors of micro beams and plates based on the MCST [30-35]. More recently, the MSCT has been applied to explore FGM microstructures with porosities. Shafiei et al. [36] developed a size- dependent nonlinear Euler-Bernoulli microbeam that accounted for nonlinear vibration behavior of imperfect FG microbeam made of porous material. Shafiei and Kazemi [37] investigated the effect of porosities, small scale effect, nonlinear, FG index, etc., on nonlinear buckling behavior of micro-/nano-beam using porous material under clamped boundary conditions. Based on Mindlin plate theory and MSCT, Şimşek and Aydin [38] studied static bending and forced vibration of porous FG micro-plate under moving load. Moreover, the MSCT also was employed for free vibration analysis of magneto elastic porous FG circular nanoplate by Hosseini et al. [39]. In this study, they employed the first order shear theory to predict the natural frequencies of the circular nanoplate using the differential quadrature method. According to the aforementioned literatures, it can be seen that few size-dependent numerical

model for FG micro-plate including porosities have been developed. Additionally, the isogeometric analysis (IGA) [40] has proved its ability in combining with non-classical continuum theories through a number of proposed size-dependent IGA finite element models [41-43].

To the best knowledge of the authors, there is no study on thermal buckling and post-buckling behaviors of FG micro-plate with porosities on the basis of modified couple stress theory and IGA available in the literature. In this article, a nonlinear size-dependent numerical solution for FG micro-plate with porosities is first established to fill this gap. Based on the proposed seventh-order shear deformation plate theory and the nonlinear von-Kármán strain, the governing equations are derived using Hamilton's principle. The MCST is employed to study the size-dependent behaviors of FG micro-plate. Moreover, the effects of porosities on thermal buckling and post-buckling responses are investigated for even, uneven and logarithmic-uneven distribution of porosities through the thickness's direction, where the material properties are calculated using the modified rule of mixture assumption. Also, the effects of material length scale parameter, porosities volume fraction, type of temperature rise, boundary conditions, FG index and length to thickness ratio on thermal buckling and post-buckling behaviors of FG micro-plate with porosities are investigated in details.

2. Basis formulations

2.1. Material properties

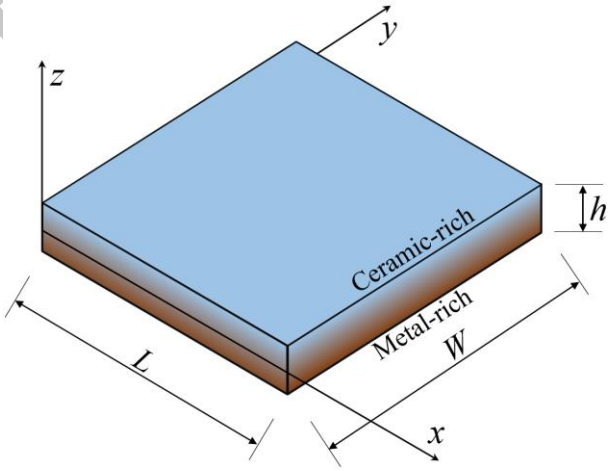

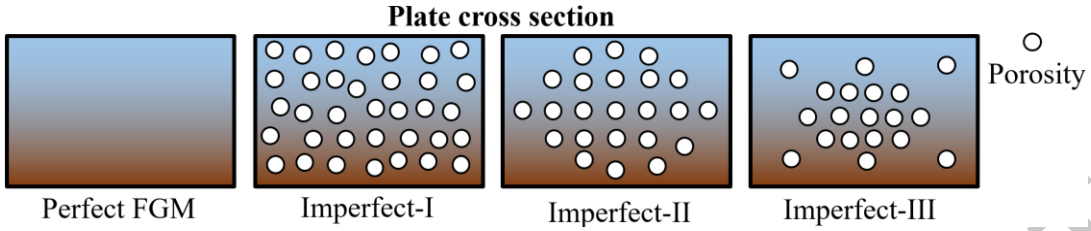

Fig. 1. Porosity models of porous micro-plate

As shown in Fig. (1), the perfect and imperfect FG rectangular micro-plate with length *L*, width *W* and height *h* are considered. The plate is assumed to be made of fully ceramic (*c*) on the top surface and fully metal on the bottom surface. This study investigates three porosities models that are Imperfect-I, -II and -III. The porosity in Imperfect-I model varies even across the thickness direction, whereas Imperfect-II denotes uneven and Imperfect-III represents logarithmic uneven distribution of porosity. The effective material properties of FG micro-plate are defined based on the modified rule of mixture [9, 10]. Hence, the effective Young's modulus $E(z)$, Poisson's ratio $\nu(z)$ and thermal expansion $\alpha(z)$ coefficient for Imperfect-I, -II and -III can be written in following form:

$$\text{Imperfect-I:}\begin{cases} E(z)=\left(E_c-E_m\right)\left(\dfrac{1}{2}+\dfrac{z}{h}\right)^n+E_m-\dfrac{\xi}{2}\left(E_c+E_m\right) \\ \nu(z)=\left(\nu_c-\nu_m\right)\left(\dfrac{1}{2}+\dfrac{z}{h}\right)^n+\nu_m-\dfrac{\xi}{2}\left(\nu_c+\nu_m\right) \\ \alpha(z)=\left(\alpha_c-\alpha_m\right)\left(\dfrac{1}{2}+\dfrac{z}{h}\right)^n+\alpha_m-\dfrac{\xi}{2}\left(\alpha_c+\alpha_m\right) \end{cases} \tag{1}$$

$$\text{Imperfect-II:}\begin{cases} E(z)=\left(E_c-E_m\right)\left(\dfrac{1}{2}+\dfrac{z}{h}\right)^n+E_m-\dfrac{\xi}{2}\left(1-\dfrac{2|z|}{h}\right)\left(E_c+E_m\right) \\ \nu(z)=\left(\nu_c-\nu_m\right)\left(\dfrac{1}{2}+\dfrac{z}{h}\right)^n+\nu_m-\dfrac{\xi}{2}\left(1-\dfrac{2|z|}{h}\right)\left(\nu_c+\nu_m\right) \\ \alpha(z)=\left(\alpha_c-\alpha_m\right)\left(\dfrac{1}{2}+\dfrac{z}{h}\right)^n+\alpha_m-\dfrac{\xi}{2}\left(1-\dfrac{2|z|}{h}\right)\left(\alpha_c+\alpha_m\right) \end{cases} \tag{2}$$

$$\text{Imperfect-III:}\begin{cases} E(z)=\left(E_c-E_m\right)\left(\frac{1}{2}+\frac{z}{h}\right)^n+E_m-\log\left(1+\frac{\xi}{2}\right)\left(1-\frac{2|z|}{h}\right)\left(E_c+E_m\right) \\ \nu(z)=\left(\nu_c-\nu_m\right)\left(\frac{1}{2}+\frac{z}{h}\right)^n+\nu_m-\log\left(1+\frac{\xi}{2}\right)\left(1-\frac{2|z|}{h}\right)\left(\nu_c+\nu_m\right) \\ \alpha(z)=\left(\alpha_c-\alpha_m\right)\left(\frac{1}{2}+\frac{z}{h}\right)^n+\alpha_m-\log\left(1+\frac{\xi}{2}\right)\left(1-\frac{2|z|}{h}\right)\left(\alpha_c+\alpha_m\right) \end{cases} \quad (3)$$

In which, n is the gradient index or power law index that define the variation of material properties though the z-direction. ξ is porosity volume fraction (porosity parameter). It is noting that setting $\xi = 0$ for FG micro-plate without porosities (Perfect FGM).

Fig. 2 illustrates the variation of Young's modulus across the thickness of AL/AL_2O_3 FG micro-plate having a porosity volume fraction $\xi = 0.2$. It can be seen that n is power law index that is taken such as $0 \le n \le \infty$. The micro-plate becomes the pure ceramic plate as n = 0 or the pure metal plate as $n = \infty$, respectively. Also, Fig. 3 plots Young's modulus of perfect and imperfect AL/AL_2O_3 FG micro-plate for power index n = 1 and n = 5. With the existence of porosities, the Young's modulus magnitude of Imperfect types decreases and becomes lower than that of Perfect FGM, in which the lowest magnitude is obtained in Imperfect-I. However, Young's modulus magnitude of Imperfect-II and -III are nearly equal each other and coincide with that of Perfect FGM at the bottom and top surfaces. As it can be seen, Young's modulus of Imperfect-II is slightly lower than that of Imperfect-III. Especially, in the middle surface, Young's modulus magnitude of Imperfect-I and -II are exactly equal.

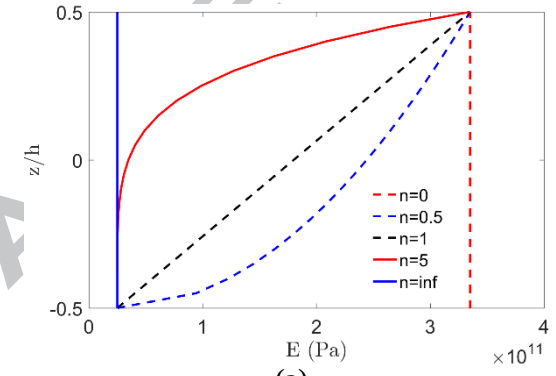

(a)

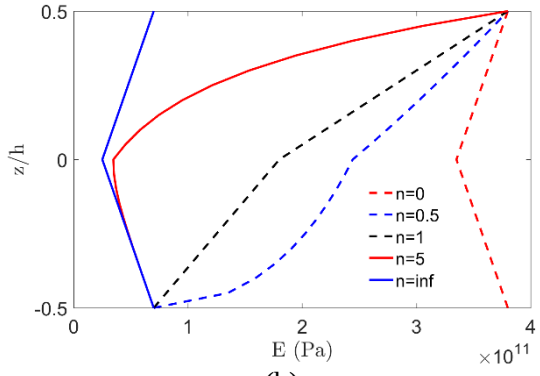

(b)

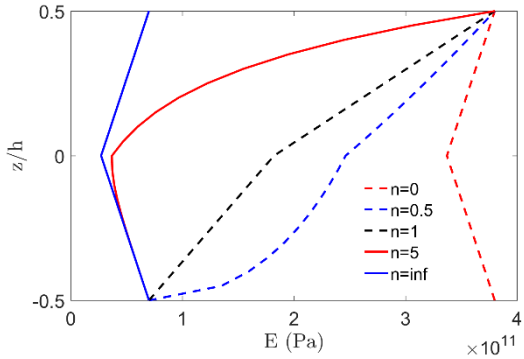

(c)

Fig. 2. The effective Young's modulus of AL/AL_2O_3 FGM micro-plate with porosity parameter $\xi = 0.2$: (a) Imperfect-I, (b) Imperfect-II and (c) Imperfect-III

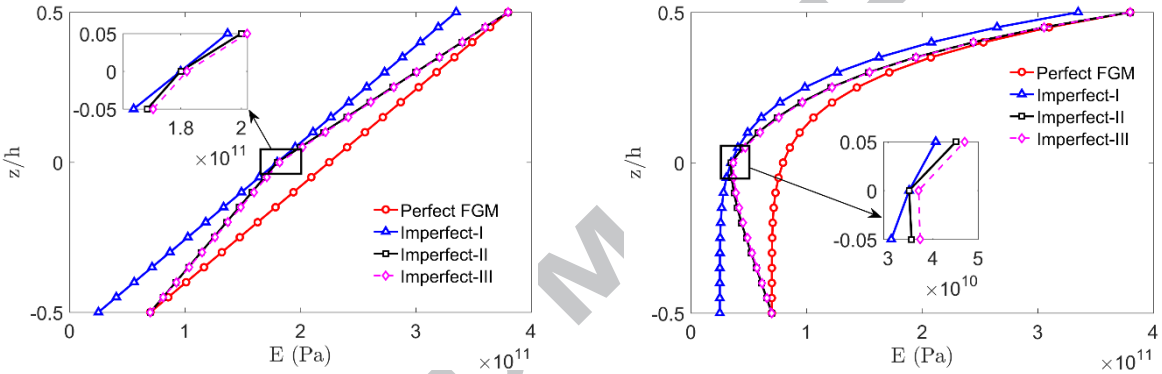

Fig. 3. Comparison of Young's modulus across the thickness of Perfect and Imperfect AL/AL_2O_3 FGM micro-plate with $\xi = 0.2$: Power index n = 1 (left) and n = 5 (right).

2.2. A size-dependent model for FGM micro-plate having porosities.

The displacement field of an arbitrary point $\mathbf{u} = \{u, v, w\}^T$ in plate domain $V = \Omega \mathbf{x}\left(-\frac{h}{2}, \frac{h}{2}\right)$ can be defined using the generalized shear deformation plate theory as [44-46]:

$$\begin{aligned} u(x,y,z) &= u_0(x,y) - z\frac{\partial w_0(x,y)}{\partial x} + f(z)\beta_x(x,y) \\ v(x,y,z) &= u_0(x,y) - z\frac{\partial w_0(x,y)}{\partial y} + f(z)\beta_y(x,y) \quad ; \left(\frac{-h}{2} \le z \le \frac{h}{2}\right) \\ w(x,y,z) &= w_0(x,y) \end{aligned} \tag{4}$$

Where β_x and β_y denote the rotations of a point of mid-plane around the y-axis and x-axis of cross-sections in x-z and y-z planes, respectively. A seventh-order function $f(z) = z - z^3/h^2 - z^5/h^4 + (4z^7)/(7h^6)$ is chosen as the distributed function, and its first derivative is $f'(z) = 1 - (3z^2)/h^2 -$

$(5z^4)/h^4 + (4z^6)/h^6$. It is clearly that the values of function $f'(z)$ are zero at $z = \pm h/2$, therefore the transverse shear stresses automatically vanish on the top and bottom surfaces of plate.

According to the modified couple stress theory developed by Yang et al. [26], the virtual strain energy of Perfect and Imperfect FGM micro-plate is written as:

$$\delta U = \int_V (\sigma_{ij}\delta\varepsilon_{ij} + m_{ij}\delta\chi_{ij})\mathrm{d}V \tag{5}$$

In which the right hand side of Eq. (5) contains two terms that defined the classical theory (first term) and the modified couple stress theory (second term). The notations σ_{ij}, ε_{ij}, m_{ij}, χ_{ij} are the components of the symmetric stress tensor , Green strain tensor, couple stress moment tensor and the symmetric curvature tensor, respectively, which are defined as:

$$\varepsilon_{ij} = \frac{1}{2}\left(\frac{\partial u_i}{\partial x_j} + \frac{\partial u_j}{\partial x_i} + \frac{\partial u_k}{\partial x_i}\frac{\partial u_k}{\partial x_j}\right) \tag{6}$$

$$\chi_{ij} = \frac{1}{2}\left(\frac{\partial \theta_i}{\partial x_j} + \frac{\partial \theta_j}{\partial x_i}\right) \tag{7}$$

$$\theta_i = \frac{1}{2}curl(u_i) \tag{8}$$

$$\sigma_{ij} = C_{ijkl}\varepsilon_{kl} \tag{9}$$

$$m_{ij} = 2G\ell^2\chi_{ij} \tag{10}$$

where C_{ijkl} , G and ℓ are elasticity constants, the shear module, the material length scale parameter, repectively. u_i and θ_i are the components of displacement and rotations, respectively.

By substituting Eq. (4) into Eq. (6), the nonlinear Von-Kármán strain-displacement relations are obtained as:

$$\begin{aligned} \boldsymbol{\varepsilon} &= \left\{\varepsilon_x\ \varepsilon_y\ \gamma_{xy}\right\}^T = \boldsymbol{\varepsilon}_0 + z\boldsymbol{\kappa}_1 + f(z)\boldsymbol{\kappa}_2 \\ \boldsymbol{\gamma} &= \left\{\gamma_{xz}\ \gamma_{yz}\right\}^T = f'(z)\boldsymbol{\varepsilon}_s \end{aligned} \tag{11}$$

where

$$\boldsymbol{\varepsilon}_0 = \boldsymbol{\varepsilon}_0^L + \boldsymbol{\varepsilon}_0^{NL} = \begin{Bmatrix} u_{0,x} \\ v_{0,y} \\ u_{0,y} + v_{0,x} \end{Bmatrix} + \frac{1}{2}\begin{Bmatrix} w_{0,x}^2 \\ w_{0,y}^2 \\ 2w_{0,x}w_{0,y} \end{Bmatrix}$$
$$\boldsymbol{\kappa}_1 = -\begin{Bmatrix} w_{0,xx} \\ w_{0,yy} \\ 2w_{0,xy} \end{Bmatrix};\ \boldsymbol{\kappa}_2 = \begin{Bmatrix} \beta_{x,x} \\ \beta_{y,y} \\ \beta_{x,y} + \beta_{y,x} \end{Bmatrix};\ \boldsymbol{\varepsilon}_s = \begin{Bmatrix} \beta_x & \beta_y \end{Bmatrix}^T \tag{12}$$

It is noted that $\boldsymbol{\varepsilon}_0^{NL}$ is the nonlinear components of in-plane, which can be rewritten as follows:

$$\boldsymbol{\varepsilon}_0^{NL} = \frac{1}{2}\mathbf{A}_\theta\boldsymbol{\theta} = \begin{bmatrix} w_{0,x} & 0 \\ 0 & w_{0,y} \\ w_{0,y} & w_{0,x} \end{bmatrix}\begin{Bmatrix} w_{0,x} \\ w_{0,y} \end{Bmatrix} \tag{13}$$

According to Eq. (4) and Eq. (8), we obtain the components of rotation vector as:

$$\begin{aligned} \theta_x &= \frac{1}{2}\left(\frac{\partial w}{\partial y} - \frac{\partial v}{\partial z}\right) = \frac{1}{2}\left(2w_{0,y} - f'(z)\beta_y\right) \\ \theta_y &= \frac{1}{2}\left(\frac{\partial u}{\partial z} - \frac{\partial w}{\partial x}\right) = \frac{1}{2}\left(-2w_{0,x} + f'(z)\beta_x\right) \\ \theta_z &= \frac{1}{2}\left(\frac{\partial v}{\partial x} - \frac{\partial u}{\partial y}\right) = \frac{1}{2}\left(\left(v_{0,x} - u_{0,y}\right) + f(z)\left(\beta_{y,x} - \beta_{x,y}\right)\right) \end{aligned} \tag{14}$$

Then, substituting Eq. (14) into Eq. (7), we can obtain the following components of curvature vector:

$$\begin{aligned} \boldsymbol{\chi}^b &= \begin{Bmatrix} \chi_x^b & \chi_y^b & \chi_{xy}^b & \chi_z^b \end{Bmatrix}^T = \boldsymbol{\chi}_1^b + f'(z)\boldsymbol{\chi}_2^b \\ \boldsymbol{\chi}^s &= \begin{Bmatrix} \chi_{xz}^s & \chi_{yz}^s \end{Bmatrix}^T = \boldsymbol{\chi}_0^s + f(z)\boldsymbol{\chi}_1^s + f''(z)\boldsymbol{\chi}_2^s \end{aligned} \tag{15}$$

where

$$\boldsymbol{\chi}_1^b = \frac{1}{2}\begin{Bmatrix} 2w_{0,xy} \\ 2w_{0,xy} \\ \left(w_{0,yy} - w_{0,xx}\right) \\ 0 \end{Bmatrix};\ \boldsymbol{\chi}_2^b = \frac{1}{4}\begin{Bmatrix} -2\beta_{y,x} \\ 2\beta_{x,y} \\ \beta_{x,x} - \beta_{y,y} \\ 2\left(\beta_{y,x} - \beta_{x,y}\right) \end{Bmatrix}$$
$$\boldsymbol{\chi}_0^s = \frac{1}{4}\begin{Bmatrix} v_{0,xx} - u_{0,xy} \\ v_{0,xy} - u_{0,yy} \end{Bmatrix};\ \boldsymbol{\chi}_1^s = \frac{1}{4}\begin{Bmatrix} \beta_{y,xx} - \beta_{x,xy} \\ \beta_{y,xy} - \beta_{x,yy} \end{Bmatrix};\ \boldsymbol{\chi}_2^s = \frac{1}{4}\begin{Bmatrix} -\beta_y \\ \beta_x \end{Bmatrix} \tag{16}$$

It is noted that the subscripts '$,x$' '$,y$' represent the derivative of arbitrary function following x and y directions, respectively.

According to Eq. (9), the constitutive equations for the relationship between the stresses and strains of FG micro-plate with porosities are given by:

$$\begin{aligned}\boldsymbol{\sigma} &= \left\{\sigma_x \quad \sigma_y \quad \tau_{xy}\right\}^T = \mathbf{C}\left(\boldsymbol{\varepsilon} - \boldsymbol{\varepsilon}^{th}\right) \\ \boldsymbol{\tau} &= \left\{\tau_{xz} \quad \tau_{yz}\right\}^T = \mathbf{G}\boldsymbol{\gamma}\end{aligned} \tag{17}$$

Where the material matrices $\mathbf{C}$ and $\mathbf{G}$ are defined as:

$$\mathbf{C} = \frac{E(z)}{1+\nu(z)}\begin{bmatrix} \dfrac{1}{1-\nu(z)} & \dfrac{\nu(z)}{1-\nu(z)} & 0 \\ \dfrac{\nu(z)}{1-\nu(z)} & \dfrac{1}{1-\nu(z)} & 0 \\ 0 & 0 & \dfrac{1}{2} \end{bmatrix}; \quad \mathbf{G} = \frac{E(z)}{2\left(1+\nu(z)\right)}\begin{bmatrix} 1 & 0 \\ 0 & 1 \end{bmatrix} \tag{18}$$

and the thermal strain is expressed as:

$$\boldsymbol{\varepsilon}^{th} = \alpha(z)\Delta T(z)\begin{bmatrix}1 & 1 & 0\end{bmatrix}^T \tag{19}$$

where $\Delta T(z) = T(z) - T_i$ is the temperature rise, $T(z)$ and T_i are the current temperature and initial temperature, respectively.

The in-plane forces, moments, higher order forces and shear forces are expressed as

$$\begin{aligned}\begin{Bmatrix} N_{ij} \\ M_{ij} \\ P_{ij} \end{Bmatrix} &= \int_{-h/2}^{h/2} \sigma_{ij} \begin{Bmatrix} 1 \\ z \\ f(z) \end{Bmatrix} \mathrm{d}z \quad ij := x,y \\ Q_{\alpha z} &= \int_{-h/2}^{h/2} \tau_{\alpha z} f'(z) \mathrm{d}z \quad \alpha := x,y\end{aligned} \tag{20}$$

By replacing Eq. (20) into Eq. (17), the stress resultant can be expressed in matrix form as follows:

$$\hat{\boldsymbol{\sigma}} = \begin{Bmatrix} \mathbf{N}^u \\ \mathbf{M}^u \\ \mathbf{P}^u \\ \mathbf{Q}^u \end{Bmatrix} = \begin{bmatrix} \mathbf{A}^u & \mathbf{B}^u & \mathbf{E}^u & \mathbf{0} \\ \mathbf{B}^u & \mathbf{D}^u & \mathbf{F}^u & \mathbf{0} \\ \mathbf{E}^u & \mathbf{F}^u & \mathbf{H}^u & \mathbf{0} \\ \mathbf{0} & \mathbf{0} & \mathbf{0} & \mathbf{D}^{us} \end{bmatrix} \begin{Bmatrix} \boldsymbol{\varepsilon}_0 \\ \boldsymbol{\kappa}_1 \\ \boldsymbol{\kappa}_2 \\ \boldsymbol{\varepsilon}_s \end{Bmatrix} - \begin{Bmatrix} \mathbf{N}_{th} \\ \mathbf{M}_{th} \\ \mathbf{P}_{th} \\ \mathbf{0} \end{Bmatrix} = \hat{\mathbf{D}}_u \hat{\boldsymbol{\varepsilon}} - \hat{\boldsymbol{\sigma}}_0 \tag{21}$$

in which

$$\left(\mathbf{A}^u,\mathbf{B}^u,\mathbf{D}^u,\mathbf{E}^u,\mathbf{F}^u,\mathbf{H}^u\right)=\int_{-h/2}^{h/2}\left(1,z,z^2,f(z),zf(z),f^2(z)\right)\mathbf{C}\mathrm{d}z$$
$$\mathbf{D}^{us}=\int_{-h/2}^{h/2}\left[f'(z)\right]^2\mathbf{G}\mathrm{d}z \tag{22}$$

and thermal stress resultant are defined as:

$$\left\{\mathbf{N}_{th}\ \ \mathbf{M}_{th}\ \ \mathbf{P}_{th}\right\}=\int_{-h/2}^{h/2}\mathbf{C}\begin{Bmatrix}\alpha(z)\\ \alpha(z)\\ 0\end{Bmatrix}\left\{1\ \ z\ \ f(z)\right\}\Delta T\mathrm{d}z \tag{23}$$

It is assumed that the temperature varies only through the plate's thickness direction, and the temperature field is unchanged in the bottom and top surfaces of the plate. In this paper, three case temperature rise are imposed:

- When the temperature is uniformly distributed through the plate's thickness, the temperature change will be a constant and take the form $\Delta T=T-T_i$, where T_i is the initial reference temperature and T is the current temperature. Using this into Eq. (23), the critical temperature difference is given as:

$$\Delta T_{cr}=\frac{N_{cr}^T}{\tilde{X}}\ \text{ with }\tilde{X}=\int_{-h/2}^{h/2}\frac{E(z)}{1-\nu(z)}\mathrm{d}z \tag{24}$$

- In case of linear temperature rise, the temperature distribution through the plate's thickness is given by:

$$T(z)=T_m+r\Delta T_{cm} \tag{25}$$

From Eq. (23) and Eq. (25), the critical temperature difference can be derived by:

$$\Delta T_{cr}=\frac{N_{cr}^T-\tilde{X}\left(T_m-T_i\right)}{\tilde{Y}}\ \text{ with }\tilde{Y}=\int_{-h/2}^{h/2}\frac{E(z)\alpha(z)}{1-\nu(z)}\left(\frac{z}{h}+\frac{1}{2}\right)\mathrm{d}z \tag{26}$$

- For the nonlinear temperature rise, a nonlinear function depend on the thickness of FGM plate can be taken as follows [47, 48]:

$$T(z)=T_m+r\Delta T_{cm}\left(\sum_{i=0}^{\infty}\frac{r^{ni}k_{mc}^i}{ni+1}\Big/\sum_{i=0}^{\infty}\frac{k_{mc}^i}{ni+1}\right) \tag{27}$$

where $r=\left(\frac{z}{h}+\frac{1}{2}\right)$, $\Delta T_{cm}=T_c-T_m$, $k_{mc}=\frac{k_m-k_c}{k_m}$, k_c and k_m are the thermal conductivity of ceramic and metal, respectively.

From Eq. (27) and Eq. (25), the critical temperature difference in nonlinear temperature field is given by:

$$\Delta T_{cr} = \frac{N_{cr}^{T} - \tilde{Z}\left(T_m - T_i\right)}{\tilde{Z}} \quad \text{with } \tilde{Z} = \int_{-h/2}^{h/2} \frac{E(z)\alpha(z)}{1-\nu(z)} r \left(\sum_{i=0}^{\infty} \frac{r^{ni} k_{mc}^{i}}{ni+1} \Big/ \sum_{i=0}^{\infty} \frac{k_{mc}^{i}}{ni+1} \right) \mathrm{d}z \tag{28}$$

Furthermore, from Eq. (10) and Eq. (15), the couple stress moment resultant can be calculated in the following form:

$$\hat{\mathbf{m}} = \begin{Bmatrix} \mathbf{N}^c \\ \mathbf{M}^c \\ \mathbf{Q}^c \\ \mathbf{R}^c \\ \mathbf{T}^c \end{Bmatrix} = \begin{bmatrix} \mathbf{A}^c & \mathbf{B}^c & \mathbf{0} & \mathbf{0} & \mathbf{0} \\ \mathbf{B}^c & \mathbf{E}^c & \mathbf{0} & \mathbf{0} & \mathbf{0} \\ \mathbf{0} & \mathbf{0} & \mathbf{X}^c & \mathbf{Y}^c & \mathbf{T}^c \\ \mathbf{0} & \mathbf{0} & \mathbf{Y}^c & \mathbf{Z}^c & \mathbf{V}^c \\ \mathbf{0} & \mathbf{0} & \mathbf{T}^c & \mathbf{V}^c & \mathbf{W}^c \end{bmatrix} \begin{Bmatrix} \boldsymbol{\chi}_1^b \\ \boldsymbol{\chi}_2^b \\ \boldsymbol{\chi}_0^s \\ \boldsymbol{\chi}_1^s \\ \boldsymbol{\chi}_2^s \end{Bmatrix} = \hat{\mathbf{D}}_c \hat{\boldsymbol{\chi}} \tag{29}$$

where

$$\begin{aligned} \left(\mathbf{A}^c, \mathbf{B}^c, \mathbf{E}^c\right) &= \int_{-h/2}^{h/2} \left(1, f'(z), \left[f'(z)\right]^2\right) \begin{bmatrix} 2G\ell^2 & 0 & 0 & 0 \\ 0 & 2G\ell^2 & 0 & 0 \\ 0 & 0 & 2G\ell^2 & 0 \\ 0 & 0 & 0 & 2G\ell^2 \end{bmatrix} \mathrm{d}z \\ \left(\mathbf{X}^c, \mathbf{Y}^c, \mathbf{Z}^c, \mathbf{T}^c, \mathbf{V}^c, \mathbf{W}^c\right) &= \int_{-h/2}^{h/2} \left(1, f(z), \left[f(z)\right]^2, f''(z), f(z)f''(z), \left[f''(z)\right]^2\right) \begin{bmatrix} 2G\ell^2 & 0 \\ 0 & 2G\ell^2 \end{bmatrix} \mathrm{d}z \end{aligned} \tag{30}$$

with $G = \dfrac{E(z)}{2\left(1+\nu(z)\right)}$

By inserting Eq. (21) and (29) into Eq. (5), the virtual strain energy of plate is now rewritten as follows:

$$\delta U = \int_{\Omega} (\hat{\boldsymbol{\sigma}} \delta \hat{\boldsymbol{\varepsilon}} + \hat{\mathbf{m}} \delta \hat{\boldsymbol{\chi}}) \mathrm{d}\Omega \tag{31}$$

By using the principle of virtual displacement, the discrete Garlekin's weak form for post-buckling problem of FGM micro-plate in thermal environment can be established such as:

$$\int_{\Omega} \delta \hat{\boldsymbol{\varepsilon}}^{\mathrm{T}} \hat{\mathbf{D}}_u \hat{\boldsymbol{\varepsilon}} \mathrm{d}\Omega + \int_{\Omega} \delta \hat{\boldsymbol{\chi}}^{\mathrm{T}} \hat{\mathbf{D}}_c \hat{\boldsymbol{\chi}} \mathrm{d}\Omega - \int_{\Omega} \nabla^{\mathrm{T}} \delta \mathrm{w} \hat{\mathbf{N}}_0^{\mathrm{th}} \nabla \mathrm{w} \mathrm{d}\Omega = \int_{\Omega} \left(\hat{\boldsymbol{\sigma}}_0\right)^T \delta \hat{\boldsymbol{\varepsilon}} \mathrm{d}\Omega \tag{32}$$

In which $\nabla = \left[\partial/\partial x \;\; \partial/\partial y\right]^T$ is the transpose of gradient operator, and $\hat{\mathbf{N}}_0^{\mathrm{th}} = \begin{bmatrix} N_x^{th} & N_{xy}^{th} \\ N_{xy}^{th} & N_y^{th} \end{bmatrix}$ is the in-plane thermal load that is calculated according to Eq. (23).

3. NURBS-based formulation of functionally graded micro-plate with porosities

In this section, discrete equations for the present problem are derived using IGA. The appropriation of the displacement fields in terms of NURBS can be expressed as [43, 49, 50]:

$$\mathbf{u}^h = \begin{Bmatrix} u_0 \\ v_0 \\ w_0 \\ \beta_x \\ \beta_y \end{Bmatrix} = \sum_{I=1}^{mxn} \begin{bmatrix} N_I & 0 & 0 & 0 & 0 \\ 0 & N_I & 0 & 0 & 0 \\ 0 & 0 & N_I & 0 & 0 \\ 0 & 0 & 0 & N_I & 0 \\ 0 & 0 & 0 & 0 & N_I \end{bmatrix} \begin{Bmatrix} u_{0I} \\ v_{0I} \\ w_{0I} \\ \beta_{xI} \\ \beta_{yI} \end{Bmatrix} = \sum_{I=1}^{mxn} \mathbf{N}_I \mathbf{d}_I \tag{33}$$

Where $\mathbf{d}_I = \begin{Bmatrix} u_{0I} & v_{0I} & w_{0I} & \beta_{xI} & \beta_{yI} \end{Bmatrix}^T$ and $\mathbf{N}_I$ are the vector of degree of freedom associated with the control point I and the shape function, respectively.

Substituting Eq. (33) into Eq. (12), the strain components can be rewritten in matrix form as:

$$\hat{\boldsymbol{\varepsilon}} = \sum_{i=1}^{m\times n} \left(\mathbf{B}_I^L + \frac{1}{2}\mathbf{B}_I^{NL} \right) \mathbf{d}_I \tag{34}$$

And the variation of the strain components is calculate as:

$$\delta\hat{\boldsymbol{\varepsilon}} = \sum_{i=1}^{m\times n} \left(\mathbf{B}_I^L + \mathbf{B}_I^{NL} \right) \delta\mathbf{d}_I \tag{35}$$

Where $\mathbf{B}_I^L = \begin{bmatrix} \left(\mathbf{B}_I^m\right)^T & \left(\mathbf{B}_I^{b1}\right)^T & \left(\mathbf{B}_I^{b2}\right)^T & \left(\mathbf{B}_I^s\right)^T \end{bmatrix}^T$ is the linear infinitesimal strain, i.e.

$$\mathbf{B}_I^m = \begin{bmatrix} N_{I,x} & 0 & 0 & 0 & 0 \\ 0 & N_{I,y} & 0 & 0 & 0 \\ N_{I,y} & N_{I,x} & 0 & 0 & 0 \end{bmatrix}; \mathbf{B}_I^{b1} = -\begin{bmatrix} 0 & 0 & N_{I,xx} & 0 & 0 \\ 0 & 0 & N_{I,yy} & 0 & 0 \\ 0 & 0 & 2N_{I,xy} & 0 & 0 \end{bmatrix}; \mathbf{B}_I^{b2} = \begin{bmatrix} 0 & 0 & 0 & N_{I,x} & 0 \\ 0 & 0 & 0 & 0 & N_{I,y} \\ 0 & 0 & 0 & N_{I,y} & N_{I,x} \end{bmatrix}; \tag{36}$$
$$\mathbf{B}_I^s = \begin{bmatrix} 0 & 0 & 0 & N_I & 0 \\ 0 & 0 & 0 & 0 & N_I \end{bmatrix}$$

and $\mathbf{B}_I^{NL}$ is the nonlinear strain matrix that is a function of displacement:

$$\mathbf{B}_I^{NL}(\mathbf{d}) = \begin{bmatrix} \mathbf{A}_\theta \\ \mathbf{0} \end{bmatrix} \mathbf{B}_I^g \text{ with } \mathbf{B}_I^g = \begin{bmatrix} 0 & 0 & N_{I,x} & 0 & 0 \\ 0 & 0 & N_{I,y} & 0 & 0 \end{bmatrix} \tag{37}$$

Similarly, by substituting Eq. (33) into Eq. (16) the couple stress curvature components are rewritten in matrix form as:

$$\hat{\boldsymbol{\chi}} = \sum_{i=1}^{m\times n} \mathbf{B}_I^{\chi}\mathbf{d}_I \text{ where } \mathbf{B}_I^{\chi} = \left[\left(\boldsymbol{\chi}_1^b\right)^T \ \left(\boldsymbol{\chi}_2^b\right)^T \ \left(\boldsymbol{\chi}_0^s\right)^T \ \left(\boldsymbol{\chi}_1^s\right)^T \ \left(\boldsymbol{\chi}_2^s\right)^T\right]^T \tag{38}$$

In which

$$\begin{aligned}
&\mathbf{B}_I^{\chi b1} = \frac{1}{2}\begin{bmatrix} 0 & 0 & 2N_{I,xy} & 0 & 0 \\ 0 & 0 & -2N_{I,xy} & 0 & 0 \\ 0 & 0 & \left(N_{I,yy}-N_{I,xx}\right) & 0 & 0 \\ 0 & 0 & 0 & 0 & 0 \end{bmatrix};\ \mathbf{B}_I^{\chi b2} = \frac{1}{4}\begin{bmatrix} 0 & 0 & 0 & 0 & -2N_{I,x} \\ 0 & 0 & 0 & 2N_{I,y} & 0 \\ 0 & 0 & 0 & N_{I,x} & -N_{I,y} \\ 0 & 0 & 0 & -2N_{I,y} & 2N_{I,x} \end{bmatrix} \\
&\mathbf{B}_I^{\chi s0} = \frac{1}{4}\begin{bmatrix} -N_{I,xy} & N_{I,xx} & 0 & 0 & 0 \\ -N_{I,yy} & N_{I,xy} & 0 & 0 & 0 \end{bmatrix};\quad \mathbf{B}_I^{\chi s1} = \frac{1}{4}\begin{bmatrix} 0 & 0 & 0 & -N_{I,xy} & N_{I,xx} \\ 0 & 0 & 0 & -N_{I,yy} & N_{I,xy} \end{bmatrix} \\
&\mathbf{B}_I^{\chi s2} = \frac{1}{4}\begin{bmatrix} 0 & 0 & 0 & 0 & -N_I \\ 0 & 0 & 0 & N_I & 0 \end{bmatrix}
\end{aligned} \tag{39}$$

Substituting Eq. (34), (35) and Eq. (38) into Eq. (32) and eliminating the virtual displacement vector $\delta\mathbf{d}$, the matrix form of the global equilibrium equations for size-dependent thermal buckling of FGM micro-plate having porosities can be established in the following matrix form:

$$\left(\mathbf{K}_L + \mathbf{K}_{NL} - \mathbf{K}_0\right)\mathbf{d} = \mathbf{F}_{th} \tag{40}$$

where $\mathbf{K}_L = \mathbf{K}_L^u + \mathbf{K}_L^{\theta}$ and $\mathbf{K}_{NL}$ are the linear and nonlinear global stiffness matrix, respectively. $\mathbf{K}_0$ is the initial stress stiffness matrix derived from the initial in-plane thermal load, while $\mathbf{F}_{th}$ is the thermal load vector. These matrices can be defined in a clear form as:

$$\begin{aligned}
\mathbf{K}_L &= \int_\Omega \left(\mathbf{B}^L\right)^T \hat{\mathbf{D}}_u \mathbf{B}^L \mathrm{d}\Omega + \int_\Omega \left(\mathbf{B}^{\chi}\right)^T \hat{\mathbf{D}}_c \mathbf{B}^{\chi} \mathrm{d}\Omega \\
\mathbf{K}_{NL} &= \frac{1}{2}\int_\Omega \left(\mathbf{B}^L\right)^T \hat{\mathbf{D}}_u \mathbf{B}^{NL} \mathrm{d}\Omega + \int_\Omega \left(\mathbf{B}^{NL}\right)^T \hat{\mathbf{D}}_u \mathbf{B}^L \mathrm{d}\Omega + \frac{1}{2}\int_\Omega \left(\mathbf{B}^{NL}\right)^T \hat{\mathbf{D}}_u \mathbf{B}^{NL} \mathrm{d}\Omega \\
\mathbf{F}_{th} &= \int_\Omega \left(\mathbf{B}^L\right)^T \hat{\boldsymbol{\sigma}}_0 \mathrm{d}\Omega
\end{aligned} \tag{41}$$

4. Nonlinear solution procedure.

4.1 Nonlinear bending problem

In this section, the nonlinear equilibrium Eq. (37) is solved by using the Newton-Raphson technique. At a specific load level m^{th}, the residual force (imbalance force) $\mathbf{R}(\mathbf{d}^i)$ at i^{th} iteration is computed as follows:

$$\mathbf{R}\left(\mathbf{d}^i\right)=\left(\mathbf{K}_L+\mathbf{K}_{NL}\left(\mathbf{d}^i\right)-\mathbf{K}_0\right)-\mathbf{F}_{th}^m \tag{42}$$

Throughout iteration, the residual force tend to zero. When the residual force is still large enough, the displacement at $(i+1)^{\text{th}}$ iteration, is then calculated as:

$$\mathbf{d}^{i+1}=\mathbf{d}^i+\Delta\mathbf{d}^{i+1} \tag{43}$$

The increment displacement $\Delta\mathbf{d}^{i+1}$ is computed using following equation:

$$\Delta\mathbf{d}^{i+1}=-\mathbf{R}\left(\mathbf{d}^i\right)\Big/\mathbf{K}_T\left(\mathbf{d}_i\right) \tag{44}$$

In which the tangent stiffness matrix $\mathbf{K}_T$ at i^{th} iteration is defined as

$$\mathbf{K}_T\left(\mathbf{d}^i\right)=\frac{\partial\mathbf{R}\left(\mathbf{d}^i\right)}{\partial\mathbf{d}^i}=\tilde{\mathbf{K}}_{NL}+\mathbf{K}_g \tag{45}$$

Where the stiffness matrix $\tilde{\mathbf{K}}_{NL}$ contains the variables $\mathbf{d}_i$ given by:

$$\tilde{\mathbf{K}}_{NL}=\int_\Omega\left(\mathbf{B}^L+\mathbf{B}^{NL}\right)^T\hat{\mathbf{D}}_u\left(\mathbf{B}^L+\mathbf{B}^{NL}\right)\mathrm{d}\Omega+\int_\Omega\left(\mathbf{B}^\chi\right)^T\hat{\mathbf{D}}_c\mathbf{B}^\chi\mathrm{d}\Omega \tag{46}$$

And $\mathbf{K}_g$ is the geometric stiffness matrix that can be obtained from in-plane forces in Eq. (23) as follows:

$$\mathbf{K}_g=\int_\Omega\left(\mathbf{B}^g\right)^T\begin{bmatrix}N_x & N_{xy}\\ N_{xy} & N_y\end{bmatrix}\left(\mathbf{B}^g\right)\mathrm{d}\Omega \tag{47}$$

The iteration is repeated until obtaining the convergence condition of displacement as follows:

$$\frac{\left\|\mathbf{d}^{i+1}-\mathbf{d}^i\right\|}{\left\|\mathbf{d}^i\right\|}<0.01 \tag{48}$$

4.2 Nonlinear eigenvalue problem

In case of pure ceramic or metallic micro-plate under uniform temperature rise, the thermal bending moments $\mathbf{M}_{\text{th}}$ in Eq. (25) are neglected, and only membrane forces are generated. Similary, when the plate is supported with full clamped edges, the bending moments can be neutralized by support reacting moments, and the plate remains flat in pre-buckling state [51-54]. Hence, the bifurcation-type buckling is exhibited for FGM micro-plate.

Firstly, the lowest eigenvalue (load factor λ) and corresponding eigenvector can be achieved by solving the linear eigenvalue equation as follow:

$$\left(\mathbf{K}_L - \lambda \mathbf{K}_0\right)\mathbf{d} = 0 \tag{49}$$

By multiplying the load factor λ with the initial load, the critical buckling temperature is obtained. Then, the critical temperature difference ΔT_{cr} is calculated by using Eq. (24), (26) and Eq. (28) depending on different temperature rise. After linear buckling, the plate endures a large deformation, so that the load factor λ must be traced by nonlinear equilibrium equation:

$$\left(\mathbf{K}_L + \mathbf{K}_{NL} - \lambda \mathbf{K}_0\right)\mathbf{d} = 0 \tag{50}$$

Next, the eigenvector is scaled up, holding the maximum displacement as $0.1h$ for each displacement incremental step, the new nonlinear stiffness matrix $\mathbf{K}_{NL}$ is updated. In this step, the new load factor and eigenvector are obtained by solving Eq. (50). This procedure is repeated until the load factor error between two succeeding iterations is smaller than the desired error tolerance $\left(\text{tol} = 0.01\right)$. In the same way, the corresponding load factor (eigenvalues) and eigenvector can be found by increasing the maximum displacement as $0.2h$, $0.3h$, etc. and the thermal post-buckling equilibrium path may be achieved.

5. Numerical results and discussions

One of the main objectives of this section is to show the effect of the small scale and the existence of porosity on the nonlinear behaviors of FGM micro-plate under uniform, linear and nonlinear temperature distribution through the plate's thickness. The top and bottom surfaces are made of pure ceramic and pure metal, respectively. In particular, Young's modulus, Poisson's ratio, thermal expansion coefficient and thermal conductivity of AL/AL_2O_3 micro-plate are assumed to be temperature-independent and taken as E_c = 380 GPa, ν_c = 0.3, α_c = 7.4×10^{-6} 1/K, k_c = 10.4 W/m K for alumina, and E_m = 70 GPa, ν_m = 0.3, α_m = 23×10^{-6} 1/K, k_m = 204 W/m K for aluminum. In addition, the three boundary conditions used in this study are:

- Simply support with movable edge (SSSS1):

$$\begin{cases} v_0 = w_0 = \beta_y = 0 & \text{at left and right edges} \\ u_0 = w_0 = \beta_x = 0 & \text{at lower and upper edges} \end{cases}$$

- Simply support with immovable edge (SSSS2):

$$\begin{cases} u_0 = v_0 = w_0 = \beta_y = 0 & \text{at left and right edges} \\ u_0 = v_0 = w_0 = \beta_x = 0 & \text{at lower and upper edges} \end{cases}$$

- Clamped support (CCCC):

$$v = u = w = 0 \quad \text{at all edges}$$

5.1. Bending analysis

To show the accuracy of the developed approach, we study the small scale effect on the nonlinear bending of perfect FGM square micro-plate under uniform distributed load, which is incrementally applied after 20 steps to reach to $q_z = 5.4\times10^6$ N/m^2. Where the material properties of the top and bottom surfaces, respectively, are E_t = 14.4 GPa, E_b = 1.44 GPa and the Poisson's ratio of both materials are assumed to be equal as $\nu_t = \nu_b = 0.38$. The obtained dimensionless central deflection $\bar{w} = w/h$ versus load parameter $\bar{q} = q_z L^4 / \left(E_b h^4\right)$ for SSSS1 and CCCC boundary conditions are compared with those given by finite element model based on a general third-order shear deformation theory (GTPT) [55]. Fig. 4 shows a good agreement of presented results in comparison with those from GTPT for power index n = 0.5, 1 and 5. From Fig. 5, it can be seen that the load-nonlinear deflection curves of homogeneous micro-plate (n = 0) with ℓ/h = 0, 0.5 and 1 agree with those of reference solution.

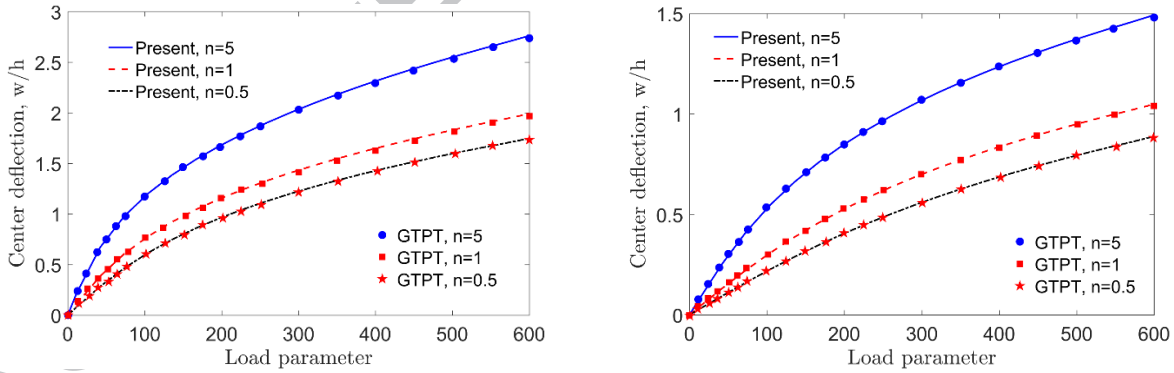

Fig. 4. Comparison of load-nonlinear deflection curves of FGM square micro-plate with $\ell/h = 0$ for various power index n under: SSSS1 (left) and CCCC (right).

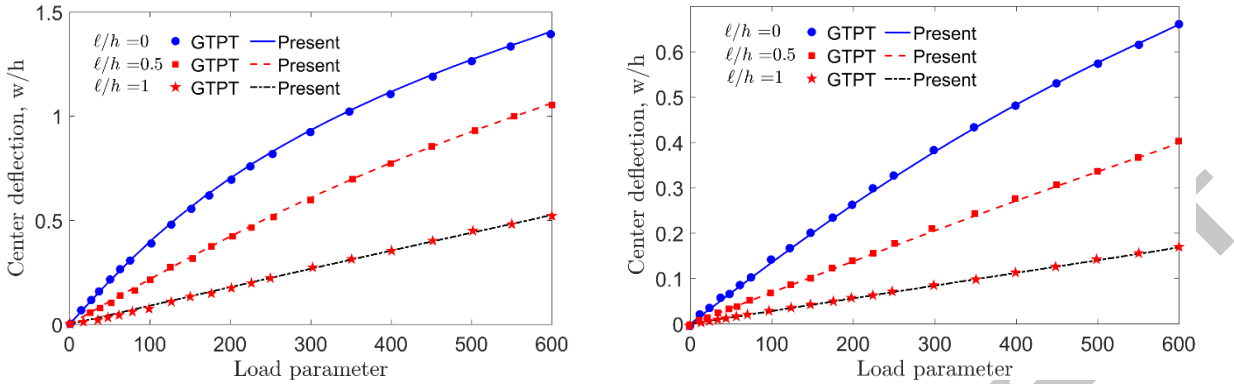

Fig. 5. Small scale effect on load-nonlinear deflection curves of homogeneous square micro-plate under: SSSS1 (left) and CCCC (right).

Next, the nonlinear bending responses of movable, immovable AL/AL_2O_3 imperfect micro-plate under linear and nonlinear temperature distribution are investigated. It can be noted that the thermal force vector on the right hand side of nonlinear Eq. (40) exists due to the effect of thermal bending moments develop together with membrane forces during temperature rise. Hence, the Newton-Raphson technique described in section 4.1 is adopted to get the temperature-displacement curves. For comparison purpose, Fig. 6 plots the load-deflection curves for simply supported plate with immovable edges under nonlinear temperature rise with power index n = 0.5, 1 and 10. Clearly, there is good agreement between the present result and the solution of Loc et al. [48], and the deflection occurs immediately when thermal load is applied. In case of n = 2 and length to thickness ratio L/h = 100, Fig. 7-9 reveal the effects of porosity on the load-deflection curves of FGM micro-plate for Imperfect-I, -II and -III by considering different porous volume fraction $\xi = 0.1, 0.2, 0.3$. These figures indicate that increase of temperature variation ΔT leads to higher dimensionless central deflection $\bar{w} = w/h$. It is also found that the linear temperature rise produces more transverse deflection in plate compared to those of nonlinear temperature rise. Moreover, for imperfect model as the porosity parameter ξ rises, the displacement decreases at the same temperature level. In Fig. 10, for comparison purpose, the temperature-displacement nonlinear curves of SSSS2 AL/AL_2O_3 square plate are illustrated for $\xi = 0.1, 0.3$ under nonlinear temperature rise. It is interesting that the deflections of imperfect model are lower than those of perfect model, the results of Imperfect-I are lower than those of Imperfect-II, -III and the deviation amplify as the porosity parameter increase from $\xi = 0.1$ to $\xi = 0.3$. However, the temperature-displacement curves of Imperfect-II are approximately equal to those of Imperfect-III. Consequently, the porosity effect on nonlinear

behavior based on temperature change of FGM micro-plate in Imperfect-I model is more significant than in the Imperfect-II and -III models.

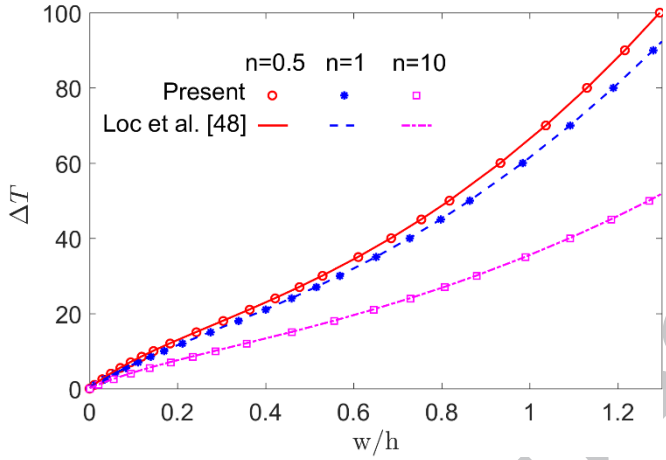

Fig. 6. Temperature-displacement of SSSS2 square (Al/Al_2O_3) plate under nonlinear temperature rise through thickness (L/h=100)

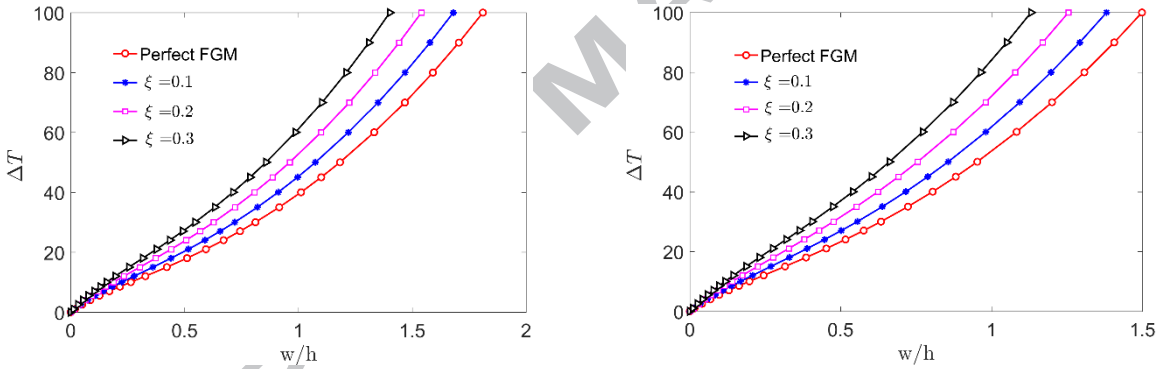

Fig. 7. Temperature-displacement curves of SSSS2 Imperfect-I FGM (Al/Al_2O_3) square plate under linear (left) and nonlinear (right) temperature rise (L/h =100, n=2)

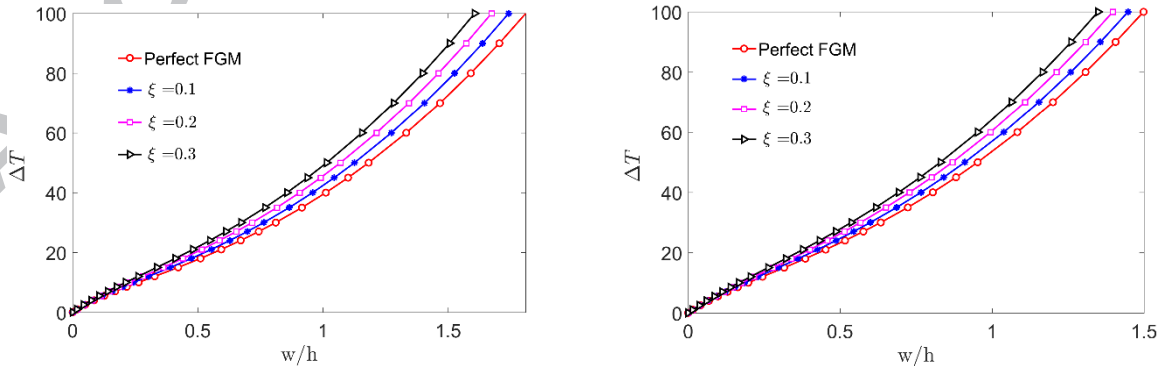

Fig. 8. Temperature-displacement curves of SSSS2 Imperfect-II FGM (Al/Al_2O_3) square plate under linear (left) and nonlinear (right) temperature rise (L/h =100, n=2)

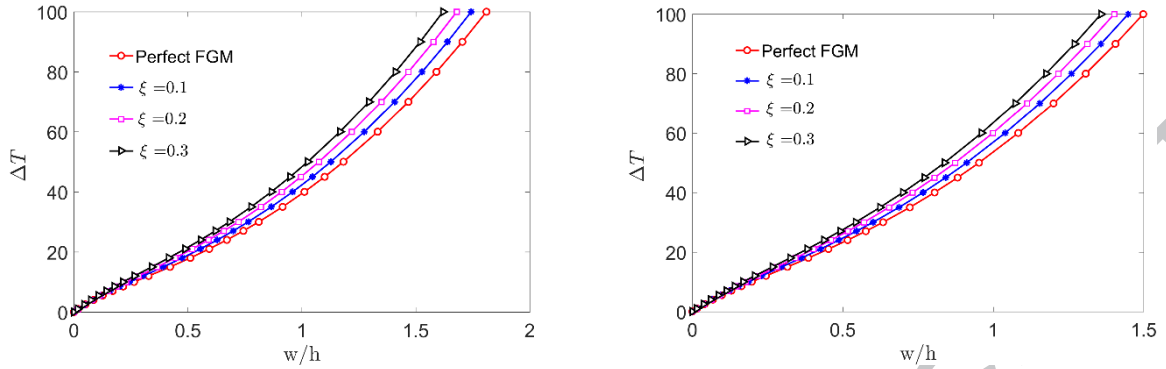

Fig. 9. Temperature-displacement curves of SSSS2 Imperfect-III FGM (Al/Al_2O_3) square plate under linear (left) and nonlinear (right) temperature rise (L/h = 100, n=2)

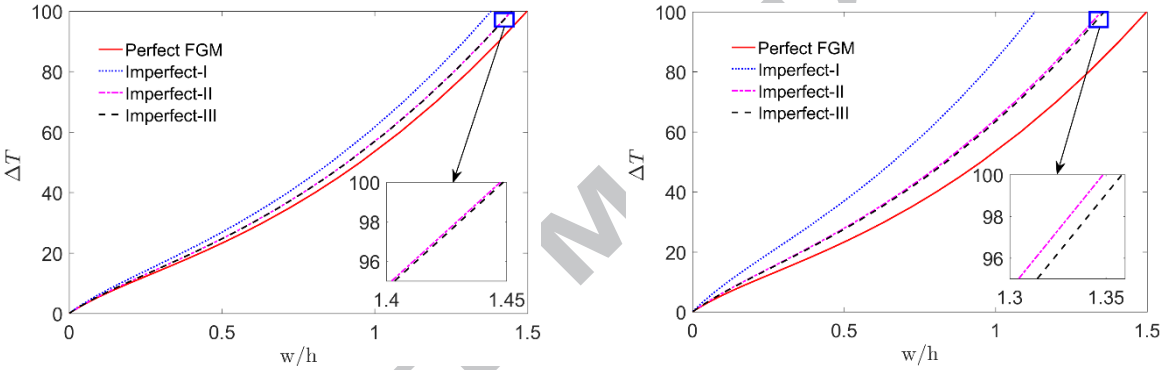

Fig. 10. Temperature-displacement curves of SSSS2 Perfect and Imperfect FGP (Al/Al_2O_3) square plate under nonlinear temperature rise through thickness (L/h = 100, n=2) with $\xi = 0.1$ (left) and $\xi = 0.3$ (right).

Subsequently, in the following example nonlinear the temperature-displacement curves of Imperfect-I, -II model are associated with the change of material length scale ratio ℓ/h as observed from Fig. 11. In this article, the material parameter is assumed to equal to $\ell = 17.6\ \mu m$, obtained from experiment work done by Lam et al. [56]. According to this figure, an increase in length scale ratio leads to a decrease in central deflection at a same temperature level and an increase in temperature variation at a same deflection level. Fig. 12 shows the effect of material power law index n on nonlinear bending behaviors of Imperfect-II FGM micro-plate predicted by conventional theory $(\ell/h = 0)$ and MCST $(\ell/h = 1)$. One can see that the plate with n = 10 has the higher deflection than the others. This is explained by the reduction of Young's modulus that results from higher metal inclusion in the imperfect FGM micro-plate.

Fig. 13 shows the nonlinear responses of imperfect AL/AL_2O_3 square micro-plate subjected to immovable simply supported boundary conditions under linear and nonlinear temperature rise. One can see that the MCST produces smaller deflection more than conventional theory owing to stiffer stiffness of micro-plate for non-zeros material length scale ratio. Furthermore, there is noteworthy differences between linear and nonlinear type. As show $(\ell/h=0.5)$ in Fig. 14, the plate bends towards the ceramic side due to the effect of thermal bending moment. It is clear that the deflections predicted by MCST $(\ell/h=0.5)$ are smaller than those predicted by classical model $(\ell/h=0)$.

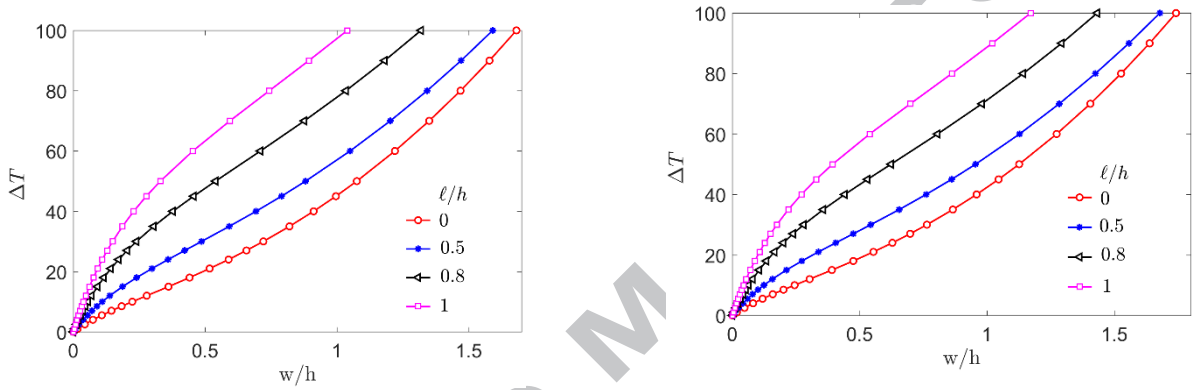

Fig. 11. Temperature-displacement curves of SSSS2 Imperfect-I (left) and Imperfect-II (right) FGP (Al/Al_2O_3) square plate under linear temperature rise through thickness (L/h = 100, n=2, temperature independent material property) with $\xi=0.1$ for different material length scale ratio ℓ/h.

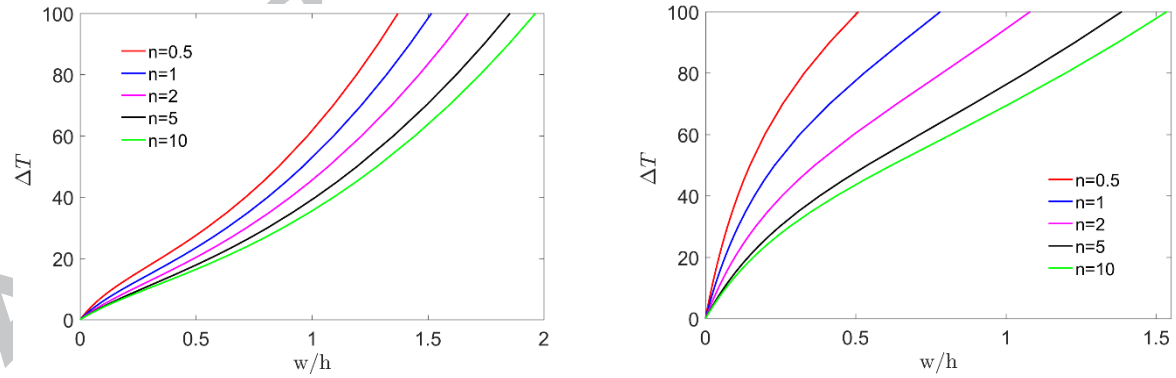

Fig. 12. Temperature-displacement curves of SSSS2 Imperfect-II FGM (Al/Al_2O_3) square micro-plate under linear temperature rise (L/h = 100, $\xi=0.2$) for length scale ratio $\ell/h=0$ (left) and $\ell/h=1$ (right).

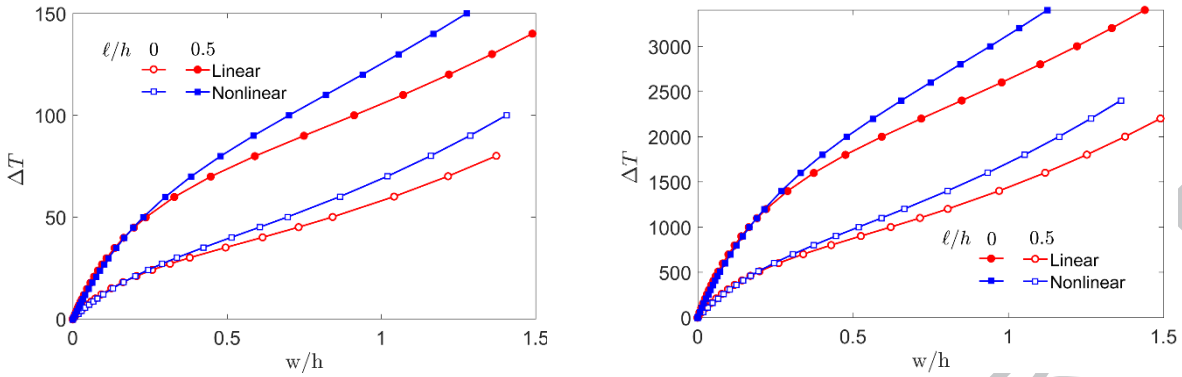

Fig. 13. Temperature-displacement curves of SSSS1 Imperfect-II FGM (Al/Al_2O_3) square micro-plate ($\xi = 0.2,\ n = 2$) for length to thickness $L/h = 100$ (left) and $L/h = 20$ (right).

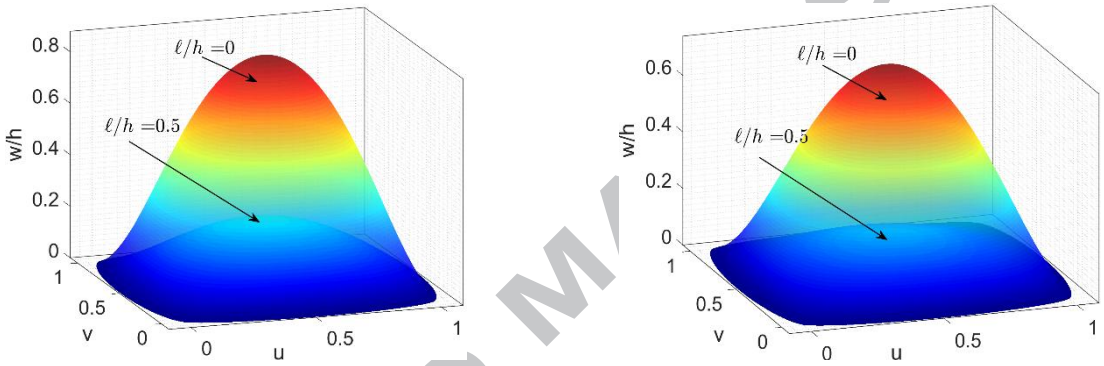

Fig. 14. Comparison of deflection of SSSS1 Perfect FGM (left) and Imperfect-I (right) FGP (Al/Al_2O_3) square micro-plate under linear temperature rise ($\xi = 0.2,\ n = 2,\ L/h = 100$) at $\Delta T = 50^0\,\mathrm{C}$.

5.2. Buckling analysis

We now analyze the accuracy of the present model through some buckling examples for perfect FGM plate $(\xi = 0)$. It is noted that the linear eigenvalue Eq. (49) is adopted in this section. Table 1 compares the critical buckling temperature of AL/AL_2O_3 square plate under uniform temperature rise for simply supported plates that are movable at all edges. The presented results agree well with those of semi-analytical method obtained by Matsunaga [57], analytical solution proposed by Javaheri and Eslami [58] and isogeometric finite element method based on third order shear deformation reported by Loc et al. [59]. To further verify the accuracy of the present method, the critical buckling temperatures of clamped AL/AL_2O_3 circular plate for L/h = 100 are given in Table 2. Through compare with the solution of Matsunaga [57], Javaheri [58] and Loc et al. [60] for linear and nonlinear temperature type, it is found that the presented numerical method can accurately predict the linear thermal buckling problem of FGM plate.

Next, a detailed study of the effect of porosity on the thermal buckling of AL/AL_2O_3 square micro-plate is carried out in Table 3. This table indicates that the increase of porosity parameter ξ leads to higher critical buckling temperature. This phenomenon is due to the reduction of the thermal expansion coefficient in Eq. (1-3) that leads to decrease the in-plane thermal load in Eq. (23) before the plate is buckled by temperature rise. It is also observed that Imperfect-II and -III models predict lower value compared to Imperfect-I model for material power index n = 0.5 and 1. Accordingly, the pattern of porosity distribution and the magnitude of porosity parameter ξ influences the buckling behavior of imperfect FGM micro-plate and the imperfect model produce higher critical buckling temperature than perfect model. Also, this inference is consistent with the findings of Barati and Zenkour [17].

The variation of material power index n leads to change in material properties that affect the change of buckling behavior of plate. Fig. 15 shows the effect of parameter n on buckling temperature of Imperfect-I and -II AL/AL_2O_3 square micro-plate under uniform temperature rise for various material length scale ratios, ℓ/h. According to this figure, for all values of ℓ/h, the buckling temperature decreases rapidly when the value n rises from 0 to 3, but this trend tends to be steady as the power index n is higher than 3. In other words, pure ceramic produces the highest thermal buckling, but the lowest result is got from pure metal. Besides, the buckling temperature increases as $\ell/h \neq 0$ and the obtained result for $\ell/h = 0.5$ is higher than the other values of ℓ/h. Moreover, for further investigation of the effect of length scale ratio ℓ/h on the thermal buckling of micro-plate, Fig. 16 shows the comparison of Imperfect-I and -II with ℓ/h vary from 0 to 1. It is noted that $\ell/h = 0$ denotes the classical theory. Similar to above-mentioned statement, as ℓ/h increases, the buckling temperature increases due to the intensification of the strength of micro-plate that come from size-dependent effect. As the ratio $\ell/h < 0.2$, the difference between classical and MCST model is not remarkable, however the size-dependent effect on thermal buckling is more considerable as the ratio $\ell/h \geq 0.2$. Fig. 16 also reveals that the deviations of results obtained from Imperfect-I and -II model enlarge as porosity volume fraction ξ and ratio ℓ/h increase.

Table 1. Critical buckling temperature of FGM square plate under uniform temperature rise.

L/h	Power index *n*	Present	HSDT [57]	CPT [58]	TSDT [58]	TSDT [59]
10	0	1618.782	1599.294	1709.911	1617.484	1618.99
	0.5	923.2382	914.1891	-	-	923.3422
	1	758.4367	749.26	794.377	757.891	758.5504
	5	679.7767	669.402	726.517	678.926	679.4828
	10	692.9872	683.211	746.927	692.519	692.8362
100	0	17.0896	17.087	17.099	17.088	17.1152
	0.5	9.6835	9.7068	-	-	9.6995
	1	7.9401	9.939	7.943	7.939	7.9538
	5	7.2608	7.259	7.265	7.26	7.2697
	10	7.4635	7.462	7.469	7.462	7.4719

Table 2. Critical buckling temperature of FGM square plate under temperature rise.

Power index n	Temp. rise	Present	TSDT [59]	FSDT [61]	FSDT [62]	CPT [62]
0	Uniform	12.7299	12.7247	12.7130	12.7120	12.7160
	Nonlinear	25.4598	25.4494	25.4260	25.9240	25.4330
0.5	Uniform	7.2132	7.2017	7.2030	7.2020	7.2040
	Nonlinear	19.0263	19.0193	18.9960	18.9960	19.0020
1	Uniform	5.9146	5.9128	5.9070	5.9060	5.9070
	Nonlinear	15.3975	15.3929	15.3770	15.3730	15.3780

Table 3. Comparison of critical buckling temperature of SSSS1 Imperfect FGM square micro-plate $(L/h=100)$ under uniform temperature rise.

L/h	ξ	*n*	Imperfect-I	Imperfect-II	Imperfect-III
0	0.1	0.5	11.292	10.719	10.693
		1	8.912	8.701	8.682
	0.2	0.5	13.474	11.894	11.778
		1	10.062	9.545	9.462
	0.3	0.5	16.624	13.230	12.942
		1	11.388	10.476	10.278
0.2	0.1	0.5	13.556	12.747	12.716
		1	10.853	10.450	10.426
	0.2	0.5	16.354	14.146	14.008
		1	12.501	11.474	11.373
	0.3	0.5	20.439	15.733	15.392
		1	14.577	12.605	12.364
0.4	0.1	0.5	20.348	18.831	18.783

	0.2	1	16.677	15.695	15.659
		0.5	24.995	20.902	20.697
		1	19.818	17.260	17.106
	0.3	0.5	31.885	23.244	22.741
		1	24.145	18.990	18.622
0.5	0.1	0.5	25.442	23.393	23.334
		1	21.044	19.628	19.583
	0.2	0.5	31.475	25.969	25.714
		1	25.305	21.600	21.406
	0.3	0.5	40.468	28.876	28.252
		1	31.321	23.778	23.315

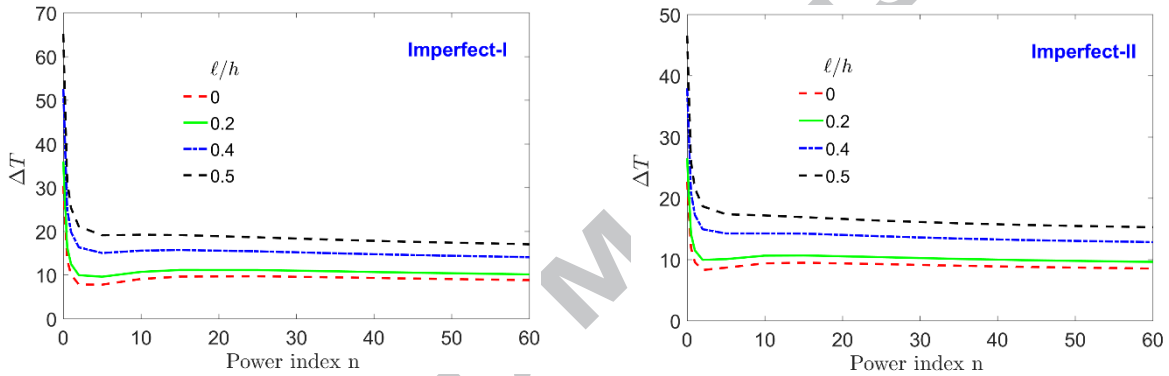

Fig. 15. Effect of power index n and length scale ratio ℓ/h on critical buckling temperature of Imperfect-I (left) and Imperfect-II (right) FGM (Al/Al_2O_3) square micro-plate ($L/h=100$, $\xi=0.2$) under uniform temperature rise.

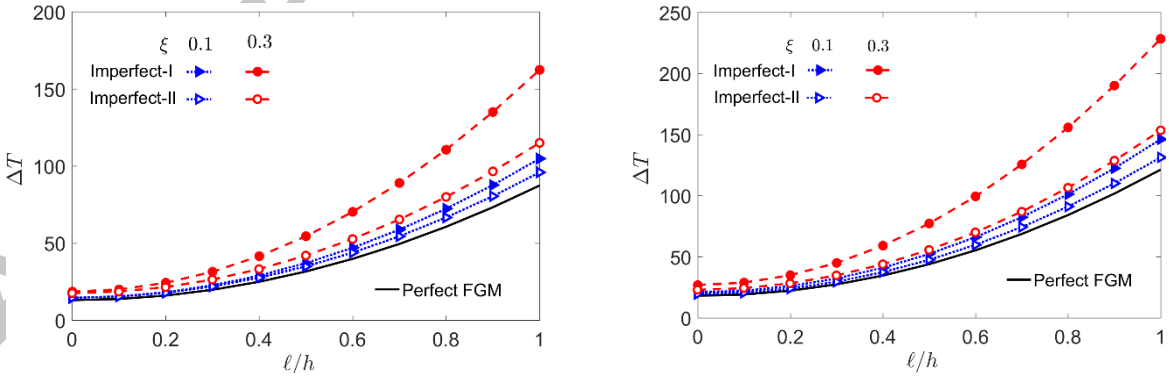

Fig. 16. Porosity volume fraction ξ and length scale ratio ℓ/h on critical buckling temperature of Imperfect-II FGM (Al/Al_2O_3) square micro-plate ($n=1$, $L/h=100$) under linear (left) and nonlinear (right) temperature rise .

5.3. Post-buckling analysis

In the following part, by eliminating the effect of thermal bending moment in Eq. (23), the post-buckling path is traced through solving nonlinear eigenvalue equation Eq. (50). Thereafter, the obtained results for all calculation parameters are presented. To verify the thermal post-buckling behavior of FGM micro-plate having porosity, the thermal post-buckling path of isotropic clamped skew plate subjected uniform temperature distribution is considered with the following material properties: E = 1 GPa, ν = 0.3, α = 10^{-6} /^{0}C, and the buckling temperature is normalized as $\bar{T} = T_{cr} E\alpha L^2 / \left(\pi^2 D\right)$, where $D = Eh^3 / 12\left(1-\nu^2\right)$ is the flexural rigidity. Fig. 17 indicates that the present curve is slightly higher than that of Loc et al. [48] and is in excellent agreement with the curve of Prabhu and Durvasula [63]. It can be seen that the seventh-order shear deformation plate theory produced more accurate result than that of Loc et al. [48] in comparison with the exact solution (Perturbation method) of Prabhu and Durvasula [63].

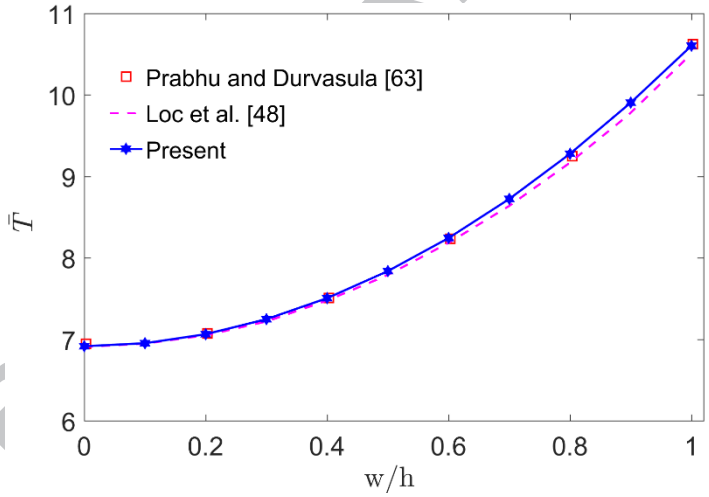

Fig. 17. Thermal post-buckling path of isotropic clamped skew plate ($L/h = 100$, angle skew $\alpha = 45^0$)

Next, Fig. 18-21 illustrate the influence of material length scale ratio, radius to thickness and porosity parameter on thermal post-buckling response of perfect and imperfect FGM clamped circular micro-plate. Fig. 18 shows the variation of the thermal post-buckling paths of plate for the length scale ratio ℓ/h = 0, 0.2, 0.4 and 0.5. It can be seen from the figure that the thermal resistance of FGM micro-plate for perfect and imperfect cases increase as ℓ/h increases, which is due to the influence of size-dependent effect $(\ell/h \neq 0)$ on the plate's stiffness based on MCST. The thermal post-buckling curves show the different between classical model $(\ell/h = 0)$

and MCST, wherein the variation is remarkable for $\ell/h=0.5$. Fig. 18 also reveals that, after bifurcation point, the maximum out-of-plane displacement increases with the increase in the critical temperature. Subsequently, there is a sudden drop in the buckling path (or thermal resistance), which follows the secondary post-buckling path. This behavior corresponds to the change of post-buckling mode shape as presented by Singha et al. [64] and Prakash et al. [53]. Furthermore, the transitional points from the primary instability to secondary instability are shifted to the right with increase in the value of ratio ℓ/h as illustrated in Fig. 18. In Fig. 19, one can see that the mode shape is symmetric with respect to middle line of plate in the primary post-buckling state, whereas the mode shape become unsymmetrical in the secondary post-buckling state. The displacement contour and the maximum displacement shift from center towards the edge of circular plate.

Fig. 20 shows the effect of the ratio R/h on thermal post-buckling path of imperfect FGM micro-plate for classical model $(\ell/h=0)$ and MCST model $(\ell/h=0.5)$. It is clearly that decrease the value of radius to thickness ratio R/h enlarges the thermal resistance of imperfect plate. Another observation from Fig. 20 is that the size-dependent effect $(\ell/h=0.5)$ leads to an increase in post-buckling critical temperature.

The variation of the thermal buckling path for various values of porosity parameter ξ also is depicted in Fig. 21. According to this figure, it can be concluded that the imperfect FGM micro-plate has higher critical buckling and post-buckling temperature than the perfect FGM micro-plate, which was concluded in Ref. [16, 65]. Furthermore, the thermal resistance increases with the rising value of porosity parameter.

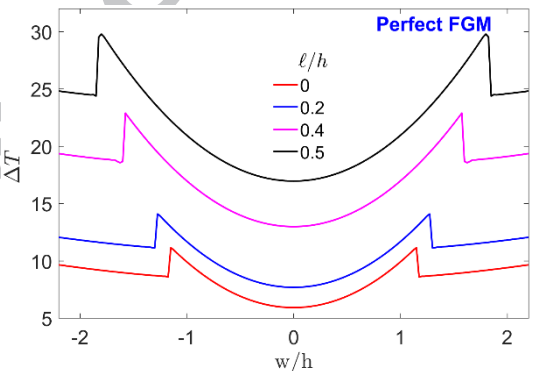

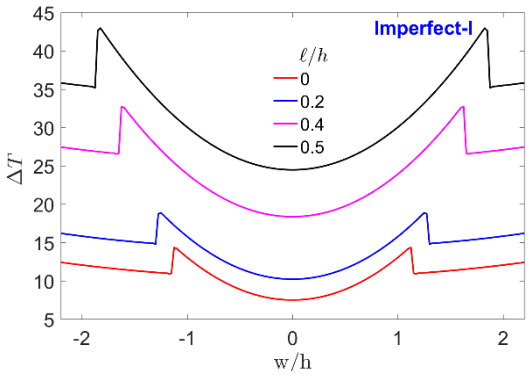

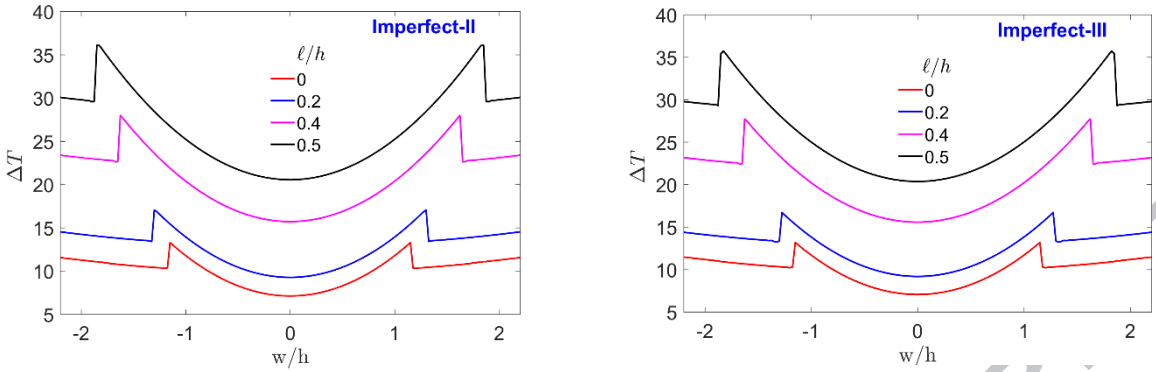

Fig. 18. Effect of length scale ratio ℓ/h on thermal post-buckling paths of Perfect FGM and Imperfect FGP (Al/Al_2O_3) clamped circular micro-plate (L/h = 100, n = 1, $\xi = 0.2$) under uniform temperature rise through thickness.

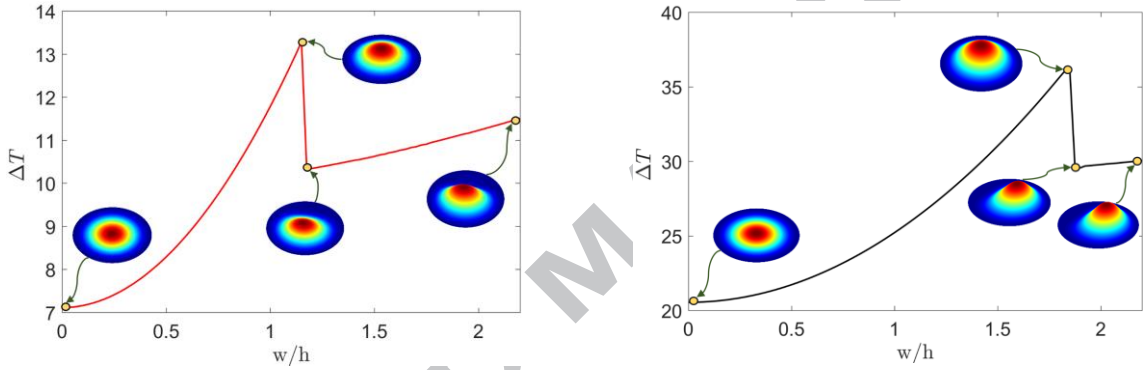

Fig. 19. Buckling mode shapes of Imperfect-II FGP (Al/Al_2O_3) clamped circular micro-plate (L/h=100, n=1, $\xi = 0.2$) for length scale ratio $\ell/h = 0$ (left) and $\ell/h = 0.5$ (right) under uniform temperature rise through thickness.

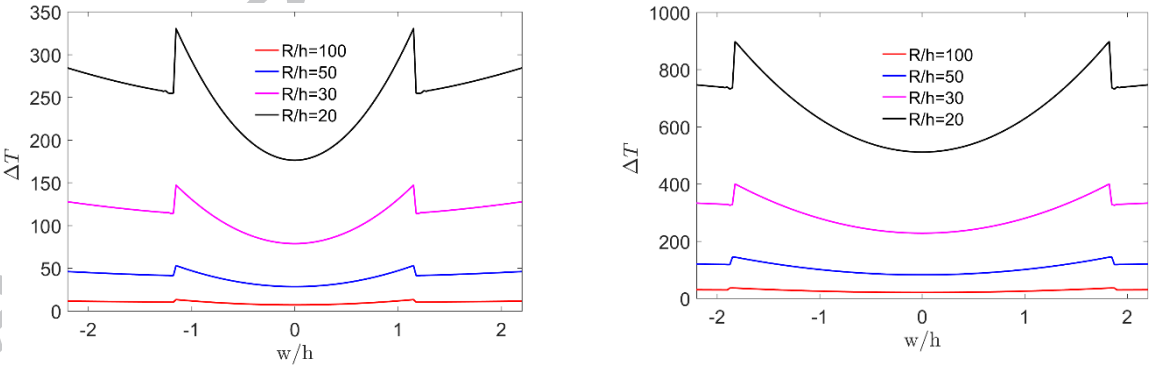

Fig. 20. Effect of radius to thickness R/h on thermal post-buckling behavior of Imperfect-II FGP (Al/Al_2O_3) clamped circular micro-plate (n = 1, $\xi = 0.2$) for length scale ratio $\ell/h = 0$ (left) and $\ell/h = 0.5$ (right) under uniform temperature rise through thickness.

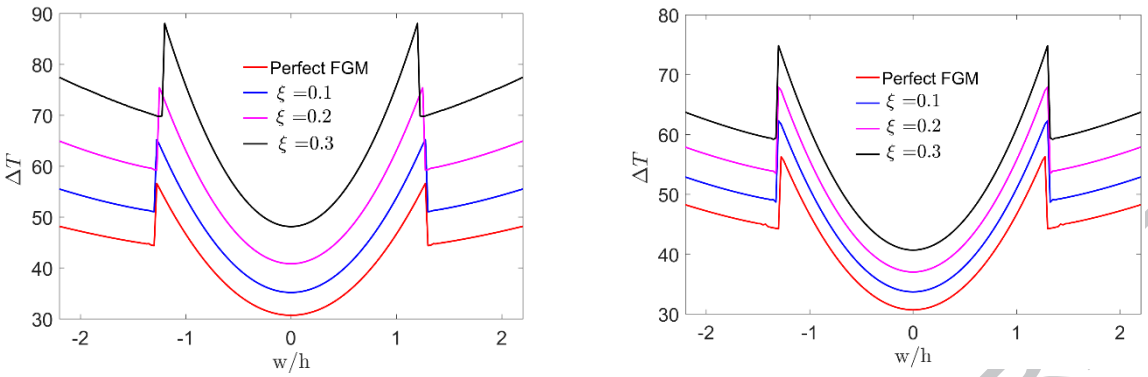

Fig. 21. Thermal post-buckling behavior of Imperfect-I (left) and Imperfect-II (right) FGP (Al/Al_2O_3) clamped circular micro-plate (L/h = 50, n = 1, $\ell/h = 0.2$) for different porous parameter ξ under uniform temperature rise through thickness.

6. Conclusion

In this paper, we have analyzed the nonlinear bending, buckling, and post-buckling behaviors of porous FGM micro-plates subjected to thermal load using IGA associated with MCST. The material properties of FGM micro-plate with even, uneven and logarithmic-uneven distribution of porosities through the thickness's direction are derived from the modified rule of mixture assumption. A proposed seventh-order shear deformation plate theory and von-Kármán assumption are utilized to establish the nonlinear governing equations that are solved by using Newton-Raphson iteration technique to acquire the nonlinear behavior of micro-plates. Also, the effect of length scale ratio, material power index, porosity distribution type, porosity parameter, temperature rise, radius to thickness and boundary conditions are discussed. Through the detailed parametric analysis, some remarkable observation are drawn as follows:

- The thermal nonlinear bending response of FGM micro-plate is caused by the existence of thermal bending moment and the extension-bending. The existence of porosity would decrease the displacement of micro-plate plate at a same temperature level, and the effect of uniform porosity model (Imperfect-I) is more remarkable than uniform (Imperfect-II) and logarithmic-uneven model (Imperfect-III). Furthermore, the size-dependent effect $(\ell/h \neq 0)$ leads to a decrease in deflection at a same temperature level and an increase in temperature variation ΔT at a same deflection level.
- The porosity model ($\xi \neq 0$) gives higher critical buckling and post-buckling temperature compared with perfect FGM micro-plate ($\xi = 0$). Also, uniform porosity model procedure more thermal resistance than even and logarithmic-uneven model.

- The critical buckling and post-buckling thermal resistance increase with the rising value of porosity parameter ξ. Besides, it is found that Imperfect-II model has higher critical buckling and post-buckling temperature than Imperfect-III model.
- The critical buckling and post-buckling temperature predicted by modified couple stress theory are higher than those derived from classical model are. The increase in material length scale ratio ℓ/h leads to increase the buckling as well as post-buckling thermal resistance.
- The radius-to-thickness ratio *R*/*h* greatly affects the mechanical response, as the thermal resistance of imperfect plates gets larger with decreasing *R*/*h* ratio.

Acknowledgements

The authors acknowledge the financial support of VLIR-OUS TEAM Project, VN2017TEA454A103, 'An innovative solution to protect Vietnamese coastal riverbanks from floods and erosion', funded by the Flemish Government.

References

[1]. Koizumi, M., FGM activities in Japan. Composites Part B: Engineering, 1997. 28(1): p. 1-4.
[2]. Miyamoto, Y., W.A. Kaysser, B.H. Rabin, A. Kawasaki, and R.G. Ford, *Processing and Fabrication*, in *Functionally Graded Materials: Design, Processing and Applications*, Y. Miyamoto, et al., Editors. 1999, Springer US: Boston, MA. p. 161-245.
[3]. Pompe, W., H. Worch, M. Epple, W. Friess, M. Gelinsky, P. Greil, U. Hempel, D. Scharnweber, and K. Schulte, Functionally graded materials for biomedical applications. Materials Science and Engineering: A, 2003. 362(1): p. 40-60.
[4]. Matsuo, S., F. Watari, and N. Ohata, Fabrication of a Functionally Graded Dental Composite Resin Post and Core by Laser Lithography and Finite Element Analysis of its Stress Relaxation Effect on Tooth Root. Dental Materials Journal, 2001. 20(4): p. 257-274.
[5]. Müller, E., Č. Drašar, J. Schilz, and W.A. Kaysser, Functionally graded materials for sensor and energy applications. Materials Science and Engineering: A, 2003. 362(1): p. 17-39.
[6]. Niino, M., K. Kisara, and M. Mori, Feasibility Study of FGM Technology in Space Solar Power Systems (SSPS). Materials Science Forum, 2005. 492-493: p. 163-170.
[7]. Zhu, J., Z. Lai, Z. Yin, J. Jeon, and S. Lee, Fabrication of ZrO2–NiCr functionally graded material by powder metallurgy. Materials Chemistry and Physics, 2001. 68(1): p. 130-135.
[8]. Wattanasakulpong, N., B. Gangadhara Prusty, D.W. Kelly, and M. Hoffman, Free vibration analysis of layered functionally graded beams with experimental validation. Materials & Design (1980-2015), 2012. 36: p. 182-190.

[9]. Wattanasakulpong, N. and V. Ungbhakorn, Linear and nonlinear vibration analysis of elastically restrained ends FGM beams with porosities. Aerospace Science and Technology, 2014. 32(1): p. 111-120.
[10]. Wattanasakulpong, N. and A.J.M. Chaikittiratana, Flexural vibration of imperfect functionally graded beams based on Timoshenko beam theory: Chebyshev collocation method. 2015. 50(5): p. 1331-1342.
[11]. Chen, D., J. Yang, and S. Kitipornchai, Elastic buckling and static bending of shear deformable functionally graded porous beam. Composite Structures, 2015. 133: p. 54-61.
[12]. Ebrahimi, F. and M. Zia, Large amplitude nonlinear vibration analysis of functionally graded Timoshenko beams with porosities. Acta Astronautica, 2015. 116: p. 117-125.
[13]. Ait Atmane, H., A. Tounsi, F.J.I.J.o.M. Bernard, and M.i. Design, Effect of thickness stretching and porosity on mechanical response of a functionally graded beams resting on elastic foundations. 2017. 13(1): p. 71-84.
[14]. Akbas, S.D.J.C.S.M., Nonlinear static analysis of functionally graded porous beams under thermal effect. 2017. 6(4): p. 399-415.
[15]. Mounaici F, B.S., Atmane HA and Tounsi A, Effect of porosity on vibrational characteristics of non-homogeneous plates using hyperbolic shear deformation theory. Win and Structures, 2016. 22: p. 429-454.
[16]. Barati, M.R. and A.M. Zenkour, Electro-thermoelastic vibration of plates made of porous functionally graded piezoelectric materials under various boundary conditions. 2018. 24(10): p. 1910-1926.
[17]. Barati, M.R., H. Shahverdi, and A.M. Zenkour, Electro-mechanical vibration of smart piezoelectric FG plates with porosities according to a refined four-variable theory. Mechanics of Advanced Materials and Structures, 2017. 24(12): p. 987-998.
[18]. Shahsavari, D., M. Shahsavari, L. Li, and B. Karami, A novel quasi-3D hyperbolic theory for free vibration of FG plates with porosities resting on Winkler/Pasternak/Kerr foundation. Aerospace Science and Technology, 2018. 72: p. 134-149.
[19]. Karami, B., D. Shahsavari, and L. Li, Temperature-dependent flexural wave propagation in nanoplate-type porous heterogenous material subjected to in-plane magnetic field. Journal of Thermal Stresses, 2018. 41(4): p. 483-499.
[20]. Cong, P.H., T.M. Chien, N.D. Khoa, and N.D. Duc, Nonlinear thermomechanical buckling and post-buckling response of porous FGM plates using Reddy's HSDT. Aerospace Science and Technology, 2018. 77: p. 419-428.
[21]. Nguyen, N.V., H.X. Nguyen, S. Lee, and H. Nguyen-Xuan, Geometrically nonlinear polygonal finite element analysis of functionally graded porous plates. Advances in Engineering Software, 2018. 126: p. 110-126.
[22]. Zhao, J., K. Choe, F. Xie, A. Wang, C. Shuai, and Q. Wang, Three-dimensional exact solution for vibration analysis of thick functionally graded porous (FGP) rectangular plates with arbitrary boundary conditions. Composites Part B: Engineering, 2018. 155: p. 369-381.
[23]. Eringen, A., On differential equations of nonlocal elasticity and solutions of screw dislocation and surface waves. J Appl Phys, 1983. 54: p. 4703–10

[24]. Mindlin, R.D. and H.F. Tiersten, Effects of couple-stresses in linear elasticity. Archive for Rational Mechanics and Analysis, 1962. 11(1): p. 415-448.
[25]. Mindlin, R.D. and N.N. Eshel, On first strain-gradient theories in linear elasticity. International Journal of Solids and Structures, 1968. 4(1): p. 109-124.

[26]. Yang, F., A.C.M. Chong, D.C.C. Lam, and P. Tong, Couple stress based strain gradient theory for elasticity. International Journal of Solids and Structures, 2002. 39(10): p. 2731-2743.
[27]. Toupin, R.A., Elastic materials with couple-stresses. Archive for Rational Mechanics and Analysis, 1962. 11(1): p. 385-414.
[28]. Koiter, W.T., Couple stresses in the theory of elasticity, I and II Nederl. Akad. Wetensch. Proc. Ser, 1964. B67: p. 17-44.
[29]. Sahmani, S., M.M. Aghdam, and T.J.C.S. Rabczuk, Nonlocal strain gradient plate model for nonlinear large-amplitude vibrations of functionally graded porous micro/nano-plates reinforced with GPLs. 2018. 198: p. 51-62.
[30]. Park, S.K. and X.L. Gao, Bernoulli–Euler beam model based on a modified couple stress theory. Journal of Micromechanics and Microengineering, 2006. 16(11): p. 2355.
[31]. Ma, H.M., X.-L. Gao, and J.N. Reddy, A Nonclassical Reddy-Levinson Beam Model Based on a Modified Couple Stress Theory. 2010. 8(2): p. 167-180.
[32]. Noori, J., S.J. Fariborz, and J.P. Vafa, A higher-order micro-beam model with application to free vibration. Mechanics of Advanced Materials and Structures, 2016. 23(4): p. 443-450.
[33]. Alinaghizadeh, F., M. Shariati, and J. Fish, Bending analysis of size-dependent functionally graded annular sector microplates based on the modified couple stress theory. Applied Mathematical Modelling, 2017. 44: p. 540-556.
[34]. Ke, L.-L., J. Yang, S. Kitipornchai, and Y.-S. Wang, Axisymmetric postbuckling analysis of size-dependent functionally graded annular microplates using the physical neutral plane. International Journal of Engineering Science, 2014. 81: p. 66-81.
[35]. Şimşek, M., M. Aydın, H.H. Yurtcu, and J.N. Reddy, Size-dependent vibration of a microplate under the action of a moving load based on the modified couple stress theory. Acta Mechanica, 2015. 226(11): p. 3807-3822.
[36]. Shafiei, N., A. Mousavi, and M. Ghadiri, On size-dependent nonlinear vibration of porous and imperfect functionally graded tapered microbeams. International Journal of Engineering Science, 2016. 106: p. 42-56.
[37]. Shafiei, N. and M. Kazemi, Nonlinear buckling of functionally graded nano-/micro-scaled porous beams. Composite Structures, 2017. 178: p. 483-492.
[38]. Şimşek, M. and M. Aydın, Size-dependent forced vibration of an imperfect functionally graded (FG) microplate with porosities subjected to a moving load using the modified couple stress theory. Composite Structures, 2017. 160: p. 408-421.
[39]. Hosseini, M., M. Mahinzare, and M. Ghadiri, Magnetic field effect on vibration of a rotary smart size-dependent two-dimensional porous functionally graded nanoplate. 2018. 29(14): p. 2885-2901.
[40]. Hughes, T.J.R., J.A. Cottrell, and Y. Bazilevs, Isogeometric analysis: CAD, finite elements, NURBS, exact geometry and mesh refinement. Computer Methods in Applied Mechanics and Engineering, 2005. 194(39): p. 4135-4195.
[41]. Nguyen, H.X., T.N. Nguyen, M. Abdel-Wahab, S.P.A. Bordas, H. Nguyen-Xuan, and T.P. Vo, A refined quasi-3D isogeometric analysis for functionally graded microplates based on the modified couple stress theory. Computer Methods in Applied Mechanics and Engineering, 2017. 313: p. 904-940.
[42]. Liu, S., T. Yu, and T.Q. Bui, Size effects of functionally graded moderately thick microplates: A novel non-classical simple-FSDT isogeometric analysis. European Journal of Mechanics - A/Solids, 2017. 66: p. 446-458.
[43]. Thanh, C.-L., P. Phung-Van, C.H. Thai, H. Nguyen-Xuan, and M. Abdel Wahab, Isogeometric analysis of functionally graded carbon nanotube reinforced composite nanoplates using modified couple stress theory. Composite Structures, 2018. 184(Supplement C): p. 633-649.

[44]. Zenkour, A.M.J.J.o.E.M., Buckling of fiber-reinforced viscoelastic composite plates using various plate theories. 2004. 50(1): p. 75-93.
[45]. Zenkour, A.M., Generalized shear deformation theory for bending analysis of functionally graded plates. Applied Mathematical Modelling, 2006. 30(1): p. 67-84.
[46]. Thai, C.H., S. Kulasegaram, L.V. Tran, and H. Nguyen-Xuan, Generalized shear deformation theory for functionally graded isotropic and sandwich plates based on isogeometric approach. Computers & Structures, 2014. 141: p. 94-112.
[47]. Samsam Shariat, B.A. and M.R. Eslami, Thermal buckling of imperfect functionally graded plates. International Journal of Solids and Structures, 2006. 43(14): p. 4082-4096.
[48]. Tran, L.V., P. Phung-Van, J. Lee, M.A. Wahab, and H. Nguyen-Xuan, Isogeometric analysis for nonlinear thermomechanical stability of functionally graded plates. Composite Structures, 2016. 140: p. 655-667.
[49]. Thai, C.H., A.J.M. Ferreira, T. Rabczuk, and H. Nguyen-Xuan, Size-dependent analysis of FG-CNTRC microplates based on modified strain gradient elasticity theory. European Journal of Mechanics - A/Solids, 2018. 72: p. 521-538.
[50]. Liu, S., T. Yu, T.Q. Bui, and S. Xia, Size-dependent analysis of homogeneous and functionally graded microplates using IGA and a non-classical Kirchhoff plate theory. Composite Structures, 2017. 172: p. 34-44.
[51]. Qatu, M.S. and A.W. Leissa, Buckling or transverse deflections of unsymmetrically laminated plates subjected to in-plane loads. AIAA Journal, 1993. 31(1): p. 189-194.
[52]. Liew, K.M., J. Yang, and S. Kitipornchai, Postbuckling of piezoelectric FGM plates subject to thermo-electro-mechanical loading. International Journal of Solids and Structures, 2003. 40(15): p. 3869-3892.
[53]. Prakash, T., M.K. Singha, and M. Ganapathi, Thermal postbuckling analysis of FGM skew plates. Engineering Structures, 2008. 30(1): p. 22-32.
[54]. Prakash, T., M.K. Singha, and M. Ganapathi, Thermal snapping of functionally graded materials plates. Materials & Design, 2009. 30(10): p. 4532-4536.
[55]. Kim, J. and J.N.J.A.M. Reddy, A general third-order theory of functionally graded plates with modified couple stress effect and the von Kármán nonlinearity: theory and finite element analysis. 2015. 226(9): p. 2973-2998.
[56]. Lam, D.C.C., F. Yang, A.C.M. Chong, J. Wang, and P. Tong, Experiments and theory in strain gradient elasticity. Journal of the Mechanics and Physics of Solids, 2003. 51(8): p. 1477-1508.
[57]. Matsunaga, H., Thermal buckling of functionally graded plates according to a 2D higher-order deformation theory. Composite Structures, 2009. 90(1): p. 76-86.
[58]. Javaheri, R. and M.R. Eslami, Thermal Buckling of Functionally Graded Plates. AIAA Journal, 2002. 40(1): p. 162-169.
[59]. Tran, L.V., C.H. Thai, and H. Nguyen-Xuan, An isogeometric finite element formulation for thermal buckling analysis of functionally graded plates. Finite Elements in Analysis and Design, 2013. 73: p. 65-76.
[60]. Tran, L.V., M.A. Wahab, and S.-E. Kim, An isogeometric finite element approach for thermal bending and buckling analyses of laminated composite plates. Composite Structures, 2017. 179: p. 35-49.
[61]. Prakash, T. and M. Ganapathi, Asymmetric flexural vibration and thermoelastic stability of FGM circular plates using finite element method. Composites Part B: Engineering, 2006. 37(7): p. 642-649.
[62]. Najafizadeh, M.M. and B. Hedayati, REFINED THEORY FOR THERMOELASTIC STABILITY OF FUNCTIONALLY GRADED CIRCULAR PLATES. Journal of Thermal Stresses, 2004. 27(9): p. 857-880.

[63]. Prabhu, M.S.S. and S. Durvasula, Thermal post-buckling characteristics of clamped skew plates. Computers & Structures, 1976. 6(3): p. 177-185.
[64]. Singha, M.K., L.S. Ramachandra, and J.N. Bandyopadhyay, Thermal postbuckling analysis of laminated composite plates. Composite Structures, 2001. 54(4): p. 453-458.
[65]. Liu, Y., S. Su, H. Huang, and Y. Liang, Thermal-mechanical coupling buckling analysis of porous functionally graded sandwich beams based on physical neutral plane. Composites Part B: Engineering, 2019. 168: p. 236-242.